CHAPTER 3

PROPERTIES OF NANOCELLULOSE EXTRACTED FROM BANANA RACHIS AND PINEAPPLE PEEL USING VARIOUS TREATMENT METHODS

3.1. Introduction

Nanocellulose (NC) describes materials that are cellulosic and have at least one dimension in the nanometre range, typically less than 300 nm. Derived from various lignocellulosic sources using different methods, NC exhibits unique properties, including greater specific surface area than cellulose at the micron scale (Liu & Kong, 2021) and negligible toxicity, with no reports of serious safety issues (Lin & Dufresne, 2014). Due to its viscous nature, low density, biodegradability, and biocompatibility, NC finds applications across diverse fields such as textiles, pharmaceuticals, and packaging and cosmetics (Ioelovich & Figovsky, 2008; Jorfi & Foster, 2015). In particular, nanocelluloses have garnered attention for their high aspect ratio (length-to-diameter ratio), low thermal expansion (Fukuzumi et al., 2009; Nogi et al., 2009), and excellent mechanical and optical properties. These attributes make them valuable in nanocomposites, paper-making, coatings, food packaging, and gas barriers (Belbekhouche et al., 2011). The potential of NC in food applications was first recognized in 1983 but remained commercially unviable because of the high expenses and energy usage (Patel, 2020). Advances in biosynthesis, structural characterization, and assembly have since spurred significant research, with publications increasing markedly in recent years. Production has expanded dramatically, with a 1000% increase in the past two years, and further growth is expected as large-scale facilities ramp up operations (Koppolu, R. 2024). Despite its broad applicability, fully addressing NC's progress in the food sector remains an enormous but exciting challenge.

The global shift toward sustainability calls for governments and institutions to adopt greener policies that mitigate the ecological footprint of fossil resources (Garcia et al., 2016; Pires et al., 2019). The European Union (EU) has demonstrated its commitment by setting renewable energy targets through directives like 2009/28/EC and 2014/15/EC (Joao et al., 2019). These directives aim to reduce greenhouse gas emissions and energy

consumption while by 2030, raising the proportion of renewable energy to 27%, significantly advancing sustainable development goals (EC, 2009; EC, 2014). One economically and environmentally viable solution is the reutilization of lignocellulosic waste, which includes agricultural residues (bagasse, leaves, bark, straw, and shells), energy crops, industrial waste, and forestry by-products (softwood and hardwood) (García et al., 2016; Pires et al., 2019). Economically, this approach promotes resource efficiency by transforming waste into valuable materials or energy sources, reducing costs associated with waste disposal, and fostering new market opportunities in bioenergy and bioproducts. It supports rural economies by providing an additional revenue stream for farmers and industries while encouraging innovation in renewable energy technologies. Environmentally, repurposing lignocellulosic waste minimizes landfill use, decreases methane emissions from organic waste decomposition, and reduces reliance on fossil fuels. It further contributes to lowering greenhouse gas emissions, conserving natural resources, and enhancing energy security. The circular economy's guiding principles are in line with the use of lignocellulosic resources, fostering a sustainable system that benefits both society and the environment.

Banana plants belong to the Musaceae family and are tall herbs in the genus *Musa* and is widely cultivated in subtropical and tropical regions. As a major commercial fruit crop, bananas rank as the world's second-largest cash crop, with an annual production exceeding 100 million tonnes (Pillai et al., 2024). India is the world's largest producer of bananas, providing over 30,000 tonnes a year, with a global production of 125 million tonnes in 2021 (Pradhan and Deo, 2019). Musa acuminata and Musa balbisiana, the two main edible species, are grown primarily for their fruit (Brown et al., 2017; Khoozani, Birch, and Bekhit, 2019). However, following harvest and post-processing, almost 60% of banana biomass is wasted, resulting in a global loss of 114.08 million metric tonnes (Alzate et al., 2021). Without effective waste management, this underutilized biomass can pose ecological challenges (Padam et al., 2012). Modern agriculture categorizes bananas alongside other cash crops like oil palm, sugarcane, pineapple, mangoes, and rice. These crops also generate significant cellulosic waste, termed agricultural biomass. Addressing this biomass is an ongoing challenge, but emerging trends emphasize its utilization for value-added uses, such as fibre composites, textiles, cattle feed, food substitutes, and renewable energy (Rosentrater et al., 2009).

Pineapple ranks as the second most harvested fruit worldwide after bananas, contributing over 20% of global fruit production, with approximately 24.8 million tons produced annually. India, Nigeria, China, Mexico, Thailand, Indonesia, the Philippines, Brazil, Costa Rica, and the Philippines are the top pineapple-producing nations (FAOstat, 2015). Around 70% of the pineapple yield is consumed fresh within the producing countries. Pineapple by-products, often underutilized, are rich in dietary fiber, phenolic compounds, minerals, and antioxidants (Rodriguez et al., 2016). These by-products can enhance the textural and functional properties of various food products. For instance, pineapple peel waste offers a valuable source of cellulose fibers. As a natural polymer and homo-polysaccharide, cellulose is abundant in nature and has diverse applications. Utilizing such by-products not only adds nutritional value but also promotes sustainable waste management practices by converting agricultural residues into functional ingredients for the food and material industries.

Cellulose nanoparticles can be synthesized in various forms, including spherical particles (Pu et al., 2007; Zhang et al., 2008), microfibrillated cellulose, which is made by mechanically breaking down cellulose fibres under high shearing forces (Teixeira et al., 2009), and rod-like, highly crystalline nanocrystals that are produced by acid hydrolysis of cellulose fibres (Azizi-Samir et al., 2005; Dufresne, 2006, 2008; Lima & Borsali, 2004). The properties of nanocellulose are influenced by hydrolysis conditions, including temperature, time (Dong et al., 1998), and the cellulose source. The generally used process involves hydrolysing delignified, hemicellulose-free cellulose with strong sulfuric acid (Bondeson et al., 2006; Nickerson & Habrle, 1947; Ranby, 1952). Acid hydrolysis of microcrystalline cellulose produces nanocellulose with a broad size range (Mandal & Chakrabarty, 2011). There are very limited studies on nanocellulose derived from banana rachis and pineapple peel, which are the most abundant and inexpensive agricultural waste materials. Furthermore, theses biomass resources have not been subjected to ultrasonication and high-pressure homogenisation techniques for the synthesis of nanocellulose. Also, utilization of this nanocellulose in various food application is also limited.

The hypothesis of this study was that the cellulose extracted from banana rachis and pineapple peel by employing a synergistic approach of chemical and mechanical treatments will have desirable structural, morphological, and physicochemical properties

that will be useful in food applications, This study explores the feasibility of utilizing agricultural waste as a sustainable resource for producing high-value nanocellulose materials, contributing to both waste valorization and the advancement of green technologies. For the study, nanocellulose was synthesized from banana rachis and pineapple peel using acid hydrolysis ultrasonication and high pressure homogenization. The extracted cellulose was subjected to a comprehensive process optimization to convert it into nanocellulose, ensuring maximum efficiency and yield. The optimized nanocellulose samples was meticulously characterized to evaluate their structural, morphological, and physicochemical properties. These characteristics was further analysed and compared to gain deeper insights into their potential end uses, such as Pickering emulsion, packaging, and hydrogels.

3.2. Materials and methods

3.2.1. Materials

Cellulose was extracted from fully mature (maturity index 2) banana rachis (*Musa acuminata*, 'Dwarf Cavendish') that was sourced from local farmers in Tezpur, while pineapple peels was obtained as laboratory waste from the Department of Food Engineering and Technology, Tezpur University. Tween-80 (purity >99%) along with sunflower oil and standard β-carotene (purity ≥ 93%) were procured from Sigma-Aldrich. Analytical chemicals were sourced from TCI, SRL, and Merck.

3.2.2. Methods

3.2.2.1. Ultrasonication

Cellulose was converted to nanoscale using a probe ultrasonicators (Takashi Ultrasonic Homogenizer U500, Japan) with a 6 mm probe, 250 W maximum power, and 0–100% amplitude. The process employed a frequency mode (2 s active, 2 s rest) and was performed in a 50 mL glass beaker with a cut-off temperature of 40 °C.

3.2.2.2. High pressure homogenisation

Cellulose suspension was nanosized using a high-pressure homogenizer (GEA Panda Plus 2000, Italy) under optimized condition in a 100 mL glass beaker. The homogenized

suspension was lyophilized, and the freeze-dried nanocellulose was collected and stored at 4 °C for further characterization.

3.2.3. Isolation of cellulose and nanocellulose

The isolation method reported by Oliveira et al. (2020) was followed. Briefly, 500 g of banana rachis and pineapple peel powder was degummed and degreased using 1L of ethanol (absolute) and hexane (1:2), then dried and crushed. The degreased material (400 g) was treated with 500 mL of 10% sodium hydroxide for 7 h at 25°C, then cleaned and dried overnight at 80°C. The pulp was treated with a 1:10 ratio of 65% (v/v) nitric acid and 80% (v/v) acetic acid and stirred for 20 min at 110°C. Amorphous solids were removed by decantation, followed by cleaning with water and ethanol. The material was then dried at 55°C for 12 h. To convert cellulose to nanocellulose, 147 g of cellulose was treated with 500 mL of 50% (v/v) sulfuric acid and stirred for 60 min at 45°C. Centrifugation (7800 x g) removed the acidic supernatant, followed by additional washes with distilled water. The suspension was sonicated in an ultrasonic bath until the pH reached 7.0 for dispersion. The nanocellulose was then dried at 100°C for 12 h to remove remaining water.

3.2.4. Experimental design

Optimization of process parameters for nanocellulose synthesis from banana rachis and pineapple peel was conducted using Response Surface Methodology (RSM) with a three-factor Box-Behnken design (BBD). The design prepared using Design Expert 13.0 software (Stat-Ease, Inc., MN), included independent variables: time, temperature, and concentration for ultrasonication, and pressure, passes, and concentration for high-pressure homogenization (HPH). **Table 3.1** presents the variable limits and coded levels for banana rachis, while **Table 3.2** details those for pineapple peel. The dependent variables were particle size and zeta potential. A total of 17 experimental runs were performed. Statistical analysis, including ANOVA with a p-value threshold of <0.05, assessed model significance. The process was optimized for nanocellulose yield, and model validation compared experimental results with predicted values.

Table 3.1. Independent variables and the coded levels of ultrasonication and High-pressure homogenizer for banana rachis

Independent variables	Symbol	Coded levels		
		-1	0	+1
Ultrasonication				
Time (min)	X_1	20	40	60
Temperature (°C)	X_2	40	50	60
Concentration (%)	X_3	25	35	45
High-pressure homogenization				
Pressure (Bar)	X_1	250	375	500
Passes	X_2	1	2	3
Concentration (%)	X_3	30	40	50

Table 3.2. Independent variables and the coded levels of ultrasonication and High-pressure Homogeniser for pineapple peel

Independent variables	Symbol	Coded levels		
		-1	0	+1
Ultrasonication				
Time (min)	X_1	20	40	60
Temperature (°C)	X_2	40	50	60
Concentration (%)	X_3	25	35	45
High-pressure homogenization				
Pressure (Bar)	X_1	250	375	500
Passes	X_2	1	2	3
Concentration (%)	X_3	30	40	50

3.2.5. Characterization of powdered banana rachis (BR), cellulose fibre (CF) and nanocellulose (NC)

The size of the nanocellulose was ascertained using dynamic light scattering (DLS) technology (Malvern®, Zetasizer Nano ZS, England). The substance was ultrasonically treated for 2 min after being dissolved in distilled water at 25 °C. The amount, intensity, volume, and average size of the nanostructures were used to quantify their size (Hemmati et al., 2018).

The FT-IR-ATR (attenuated total reflectance) spectra were analysed using a spectrometer (Nicolet Instrument 410 FT-IR, Thermo Scientific, USA), and the data was collected at a resolution of 4 cm^{-1} and performed in the spectral region 4000–400 cm^{-1}.

The relative crystallinity was measured utilising an X-ray diffractometer (Bruker AXS, Germany, D8 FOCUS) run at 60 kV with a scanning range of 10 to 80° (2θ). The analysis was carried out at room temperature at a step size of 0.001°. The X-ray diffractograms were used to calculate the relative crystallinity using **Eq. 3.1** (Rabek et al., 1980):

$$\text{Relative crystallinity } (\%) = \frac{A_c}{(A_c + A_a)} \times 100 \qquad \textbf{Eq. 3.1}$$

where Aa is the amorphous region and Ac is the crystalline region.

Samples were tested for thermal stability using a Thermogravimetric Analyser (TGA) (model # TG 209 F1 Libra, Make # Netzsch, Germany). Samples (6–10 mg) were heated at a rate of 10 °C min^{-1} between 30 and 600 °C. While running the instrument, 20 mL of nitrogen per minute was pumped into the system. For calculating the degradation temperature, the weight change over time (dW/dT) was plotted against temperature (°C) to create a derivative thermogravimetric (DTG) curve.

A differential scanning calorimeter (Model: DSC 214 Polyma, make: Netzsch, Germany) was used to evaluate the thermal behaviour of the cellulose. Each sample, weighing around 10 mg, was carefully placed in an aluminium concave pan with the lid inverted. The samples were heated from 30 °C to 350 °C in a nitrogen environment at a regulated rate of 10 °C per min. Important thermal data, such as the onset temperature (To), peak temperature (Tp), conclusion temperature (Tc), and enthalpy (H), were provided by the thermograms that were produced.

To analyse the samples' morphology, a field emission scanning electron microscope (JSM-7200F, JEOL, Japan) was employed. Immediately after being shattered, the liquid nitrogen-frozen samples had a thin layer of gold sprayed on them. A 10 kV accelerating voltage was used.

After placing a 10 µL drop of diluted nanocellulose suspension on a carbon-coated Cu grid and drying it under a table lamp, it was dyed for 3 min with ruthenium vapour. Transmission electron micrographs were captured using a TECNAI G2 20 S-TWIN TEM (FEI, USA) at 200 kV with 2.4 Å resolution.

Cellulose fibers from acid-hydrolysed, alkali-treated banana rachis and pineapple peel powder were analysed for morphology and dimensions using an Atomic Force Microscope (Model: NTEGRA Vita, NT-MDT) in tapping mode at ambient temperature. A sonicated, diluted cellulose suspension was deposited on an optical glass substrate, dried at room temperature, and examined, revealing detailed surface structure and dimensional characteristics.

3.2.6. Data analysis

Every experiment was conducted at least three times, and the results were presented as mean ± standard deviation of mean. Design Expert 13.0 software was used to do an ANOVA analysis on the optimisation data (Stat-Ease, Inc., MN). The data from XRD, FT-IR, TGA and DSC were treated by the software Origin Pro IBM SPSS 20.0.

3.3. Results and discussion

3.3.1. Stages of nanocellulose isolation from banana rachis

The process for isolating NC from banana rachis and pineapple peel is illustrated in **Fig. 3.1**. Chemical reagents were employed to remove non-cellulosic components of the fibers. Initially, the fibers were treated with a 2:1 mixture of hexane and ethanol for 5 hours to swell the fibers, enhancing reagent penetration (Berni et al., 2019). Sodium hydroxide treatment was then applied to remove hemicellulose and improve the solubility of lignin and hemicellulose. Subsequently, a 10:1 mixture of acetic acid and nitric acid was used at 110 °C for 20 min to bleach the lignocellulosic fibers, yielding cellulose fibers. These fibers, referred to as bleached fibers, were then hydrolysed using sulfuric acid, which

esterified the hydroxyl groups and reduced particle size. The resulting NC was washed multiple times to achieve neutrality, then sonicated in an ice bath to extract rod-shaped nanocellulose. The processing images of NC extraction is depicted in **Fig. 3.2**. This comprehensive chemical treatment efficiently isolated NC, removing unwanted components and producing high-quality rod-shaped nanocellulose. **Fig. 3.1.** Sequence of

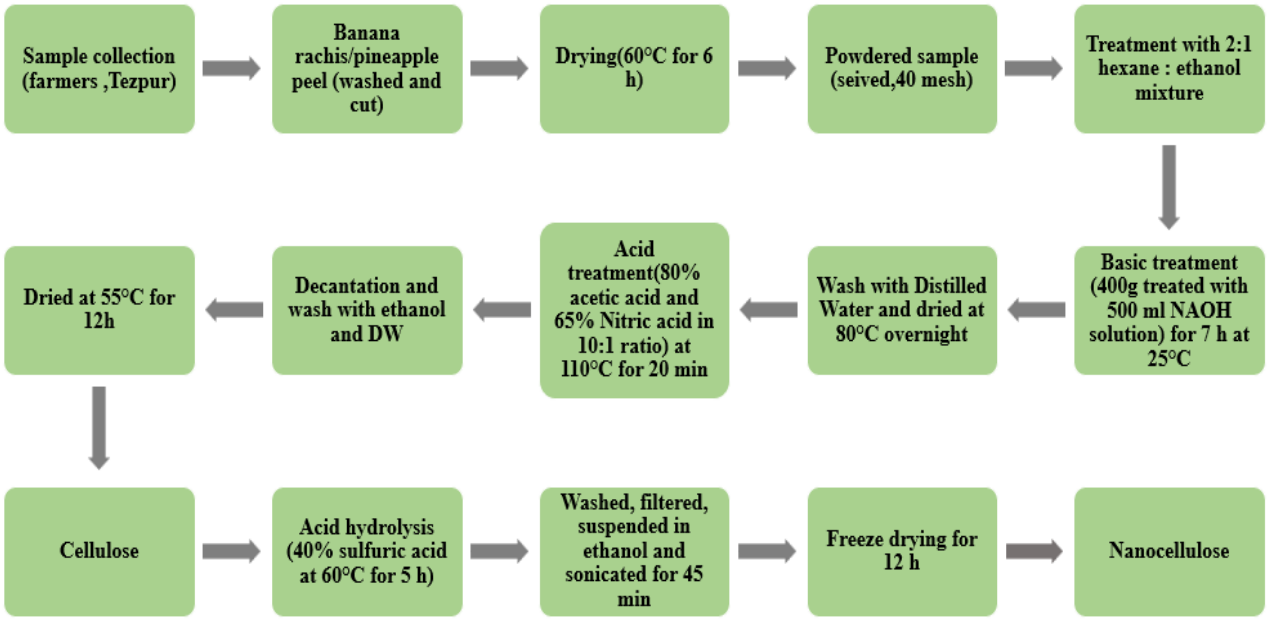

steps followed for nanocellulose isolation.

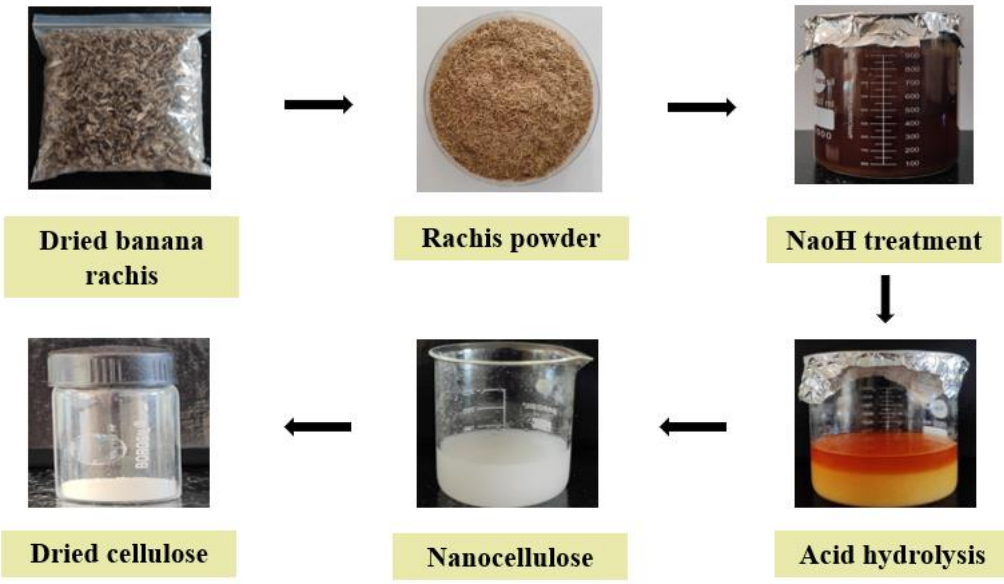

Fig. 3.2. Stages of treatment during nanocellulose isolation from banana rachis.

3.3.2. Modelling and fitting using ultrasonication (US) for banana rachis

The influence of the process parameters viz., time, temperature and concentration on particle size and zeta potential was investigated using response surface methodology. Regression analysis of the data was performed using design expert software to fit a second order polynomial quadratic equation using Box Behnken Design. The regression coefficients of individual linear, quadratic, and interaction factors were identified based on the analysis of variance. The regression coefficients were utilised to create 3-D surface plots and contour plots from the fitted polynomial equation in order to illustrate the relationship between the response and experimental levels of each factor and to determine the ideal conditions. Box Behnken Design did the experiment, and the results are displayed in the **Table 3.3**.

Table 3.3. Particle size and zeta potential obtained for the independent variables using ultrasonication

Run	Independent Variables			Response	
	Time (min)	Temperature (°C)	Concentration (%)	Particle size (nm)	Zeta potential (mV)
1	40	60	25	104	-14.8
2	40	50	35	189	-12.4
3	60	50	45	43	-8.6
4	20	50	25	117	-15.2
5	20	60	35	118	-13.4
6	20	40	35	109	-14.2
7	40	60	45	64	-9.1
8	40	40	25	122	-15.4
9	40	50	35	176	-12.2
10	40	50	35	162	-13.6
11	20	50	45	56	-9.3
12	40	50	35	156	-12.8
13	60	40	35	101	-13.1
14	40	40	45	72	-10.2
15	60	50	25	108	-14.9
16	40	50	35	172	-13.5
17	60	60	35	111	-12.7

The ANOVA table for particle size (**Table 3.4**) indicated a significant model fit ($p<0.0003$). Among the linear parameters, time and temperature were insignificant

($p>0.05$), while concentration was significant ($p<0.05$). Interaction terms were also found to be insignificant ($p>0.05$). Consequently, the final predictive equation (**Eq. 3.2**) was derived by excluding non-significant parameters ($p>0.05$), ensuring a refined model focused on key variables affecting particle size.

Table 3.4. ANOVA of particle size for quadratic model obtained for ultrasonication

Source	**Sum of Squares**	**df**	**Mean Square**	**F-value**	**p-value**	
Model	28816.99	9	3201.89	20.81	0.0003	**Significant** ***
A-Time	171.13	1	171.13	1.11	0.3267	
B-Temperature	6.13	1	6.13	0.0398	0.8475	
C-Concentration	5832.00	1	5832.00	37.90	0.0005	**
AB	0.2500	1	0.2500	0.0016	0.9690	
AC	4.00	1	4.00	0.0260	0.8765	
BC	25.00	1	25.00	0.1625	0.6989	
A²	5269.01	1	5269.01	34.24	0.0006	***
B²	2819.01	1	2819.01	18.32	0.0037	**
C²	12563.75	1	12563.75	81.64	< 0.0001	***
Lack of Fit	421.25	3	140.42	0.8562	0.5321	**not significant**
R-squared	**0.9640**					
Adj R-squared	**0.9176**					

*Significant at $p<0.1$, **Significant at $p<0.05$, ***Significant at $p<0.001$, df: degrees of freedom

Particle size = $171 - 4.625\,A - 0.875\,B - 27\,C + 0.25\,AB - 1\,AC + 2.5\,BC - 35.375\,A^2 - 25.875\,B^2 - 54.625\,C^2$ **Eq. 3.2**

As indicated by the determination coefficient (R^2) of 0.9640, 96.40% of the sample changes for the particle size optimisation efficiency were linked to the independent variables, whereas the model was unable to explain 3.60% of the total variations. The model has been tested and may work well for optimising particle size for ultrasonication, as evidenced by the lack of fit being found to be negligible equivalent to pure error ($p>0.05$).

Table 3.5. ANOVA of zeta potential for quadratic model obtained for ultrasonication

Source	**Sum of Squares**	**df**	**Mean Square**	**F-value**	**p-value**	
Model	73.13	9	8.13	29.59	< 0.0001	**Significant** ***
A-Time	0.9800	1	0.9800	3.57	0.1008	
B-Temperature	1.05	1	1.05	3.83	0.0913	*
C-Concentration	66.70	1	66.70	242.87	< 0.0001	***
AB	0.0400	1	0.0400	0.1456	0.7141	
AC	0.0400	1	0.0400	0.1456	0.7141	
BC	0.0625	1	0.0625	0.2276	0.6479	
A^2	0.0059	1	0.0059	0.0216	0.8874	
B^2	0.7164	1	0.7164	2.61	0.1503	
C^2	3.70	1	3.70	13.47	0.0080	**
Lack of Fit	0.3225	3	0.1075	0.2687	0.8455	**not significant**
R-squared	**0.9744**					
Adj R-squared	**0.9415**					

*Significant at $p<0.1$, **Significant at $p<0.05$, ***Significant at $p<0.001$, df: degrees of freedom

The ANOVA table for zeta potential (**Table 3.5**) showed a significant model fit ($p<0.0001$). While the linear parameters of time and temperature were insignificant

($p>0.05$), concentration was significant ($p<0.05$). Interaction terms were also insignificant ($p>0.05$). As a result, the final predictive equation (**Eq. 3.3**) was formulated by omitting non-significant parameters ($p>0.05$), yielding a streamlined model focused on the critical variable influencing zeta potential.

Zeta potential = - $12.9 + 0.35\ A + 0.3625\ B + 2.8875\ C - 0.1\ AB + 0.1\ AC + 0.125\ BC - 0.0375\ A^2 - 0.4125\ B^2 + 0.9375\ C^2$ **Eq. 3.3**

The determination coefficient (R^2) of 0.9744 indicates that 97.44% of the variation in zeta potential optimization efficiency was explained by the independent variables, with 2.56% unexplained by the model. The lack of fit was insignificant relative to pure error ($p>0.05$), validating the model's accuracy. This confirms the model's reliability for optimizing zeta potential during ultrasonication, ensuring robust performance in predicting outcomes.

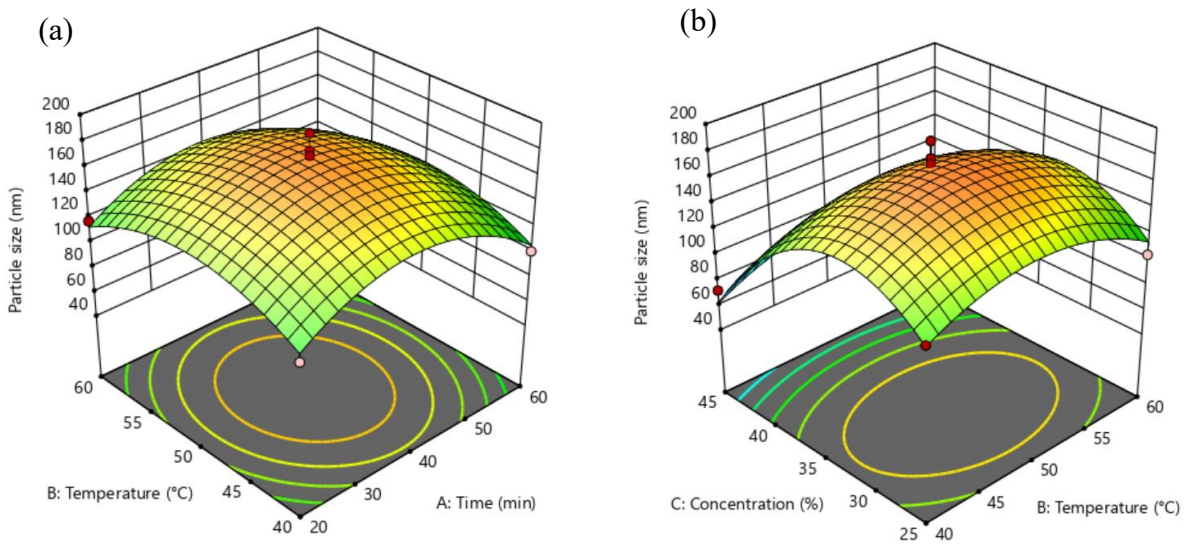

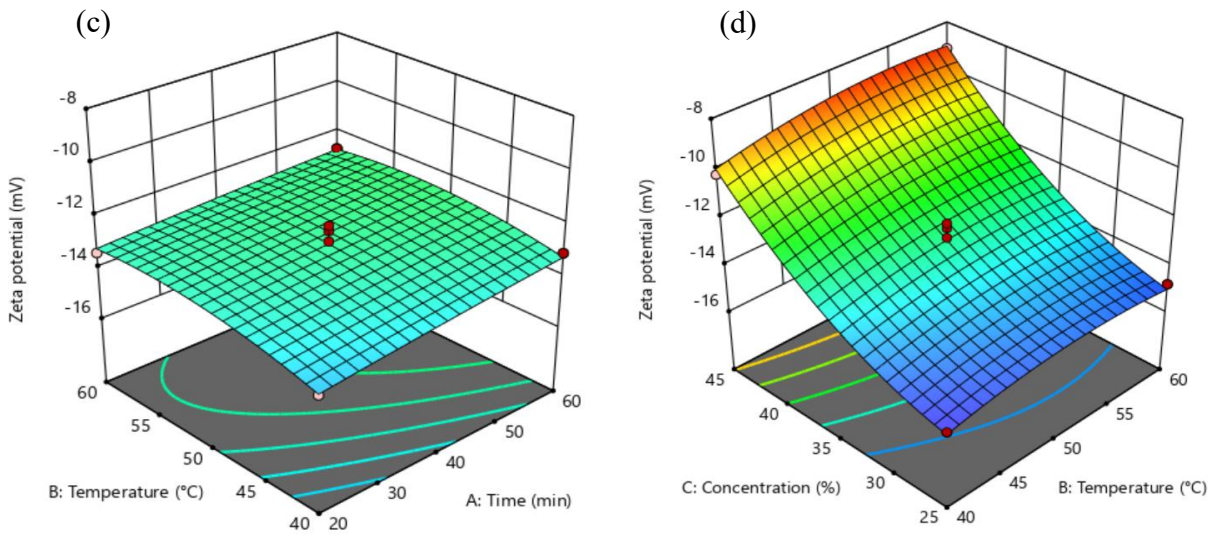

Fig. 3.3. 3D surface graphs of (a, b) particle size and (c, d) zeta potential of nanocellulose obtained by ultrasonication.

The interactive effects of independent variables on particle size and zeta potential were analysed using three-dimensional response surface profiles derived from multiple non-linear regression models. The independent variables viz., time, temperature, and concentration were plotted on the z-axis to generate 3D surface and contour graphs, facilitating the study of their effects on the dependent variables. **Fig 3.3** illustrates the interactions among time, temperature, and concentration on particle size and zeta potential. In the graph, particle size initially increased with rising time and temperature but showed a reverse trend after reaching a certain threshold. Similarly, particle size increased with higher concentrations before declining after a specific limit. For zeta potential, a slight increase was observed with increasing time and temperature, without any subsequent reversal. Additionally, zeta potential consistently increased with higher concentrations. The interaction between time and temperature demonstrated a positive effect, indicating that an increase in both parameters caused a rise in particle size. Likewise, the interaction between concentration and temperature exhibited a similar positive trend, suggesting that elevated concentration and temperature led to increased particle size. These results highlight temperature as the critical factor in optimizing particle size. For zeta potential, the interaction between time and temperature also showed a positive effect, where their combined increase resulted in higher zeta potential. Similarly, the interaction between concentration and temperature had a positive impact, demonstrating that increasing both

variables led to an enhancement in zeta potential. Overall, temperature emerged as a key determinant influencing both particle size and zeta potential during the optimization process.

Table 3.6. Optimum conditions, experimental and predicted values obtained for ultrasonication

Optimum Conditions	Coded Levels	Actual Levels	
Time (min)	-1.00	20	
Temperature (°C)	-1.00	40	
Concentration (%)	-1.00	25	
Response	Predicted Values	Experimental Values	Desirability
Particle size (nm)	120.8	**122.4**	1.00
Zeta potential (mV)	-14.5	**-14.6**	

$$\mathbf{Z=(Z_0-Z_c)/\Delta Z}$$

Where, Z and Z_0 indicate coded and actual levels of independent variables, respectively. ΔZ represents step change while Z_c indicated actual value at central point.

The process was validated using desirability analysis (**Table 3.6**), achieving the highest desirability score of 1 under optimal conditions: time of 20 min, temperature of 40 °C, and concentration of 25%. The predicted particle size and zeta potential was 120.8 nm and -14.5 mV, respectively, while experimental results were 122.4 nm for particle size and -14.6 mV for zeta potential. The close agreement between predicted and experimental values, supported by DLS data (**Fig. 3.4**), demonstrated minimal deviation. These findings confirm the validity of the optimized conditions, ensuring their reliability for further study and application in nanocellulose production.

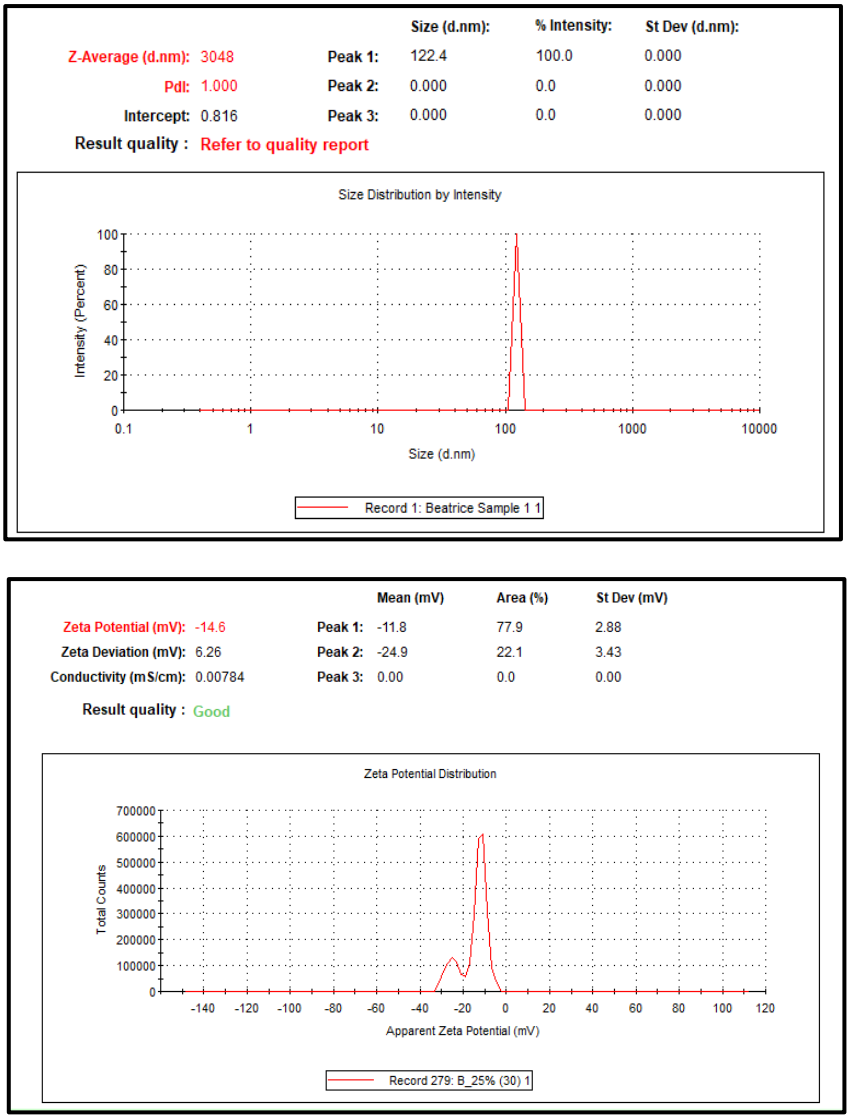

Fig. 3.4. Particle size distribution and zeta potential of the nanocellulose obtained by ultrasonication.

3.3.3. Modelling and fitting using high-pressure homogenisation (HPH) for banana rachis

The effects of process parameters viz., pressure, passes, and concentration on particle size and zeta potential were analysed using response surface methodology. Regression analysis was performed with Design Expert software, fitting a second-order polynomial quadratic equation based on Box-Behnken Design. Analysis of variance determined the regression coefficients for linear, quadratic, and interaction terms. To visualize the relationship between responses and factor levels, 3D surfaces and contour plots were generated from the fitted equation. The experimental design and corresponding responses obtained

through Box-Behnken Design are presented in **Table 3.7**, providing insights into optimizing process conditions.

Table 3.7. Particle size and zeta potential obtained for the independent variables using high-pressure homogenization

Run	Independent Variables			Response	
	Pressure (bar)	Passes	Concentration (%)	Particle size (nm)	Zeta potential (mV)
1	375	2	40	308	-9.21
2	250	2	30	321	-17.2
3	375	1	30	374	-10.6
4	375	1	50	248	-8.1
5	250	1	40	422	-14.8
6	375	3	50	402	-7.32
7	375	2	40	305	-8.74
8	500	2	50	267	-12.4
9	250	3	40	434	-12.2
10	375	3	30	209	-7.41
11	500	3	40	345	-11.6
12	375	2	40	311	-9.68
13	375	2	40	306	-10.1
14	250	2	50	353	-13.7
15	500	2	30	214	-14.6
16	375	2	40	319	-8.26
17	500	1	40	310	-10.9

The ANOVA table for particle size (**Table 3.8**) confirmed a significant model fit ($p<0.0001$). In the linear parameters, passes were insignificant ($p>0.05$), while pressure and concentration were significant ($p<0.05$). The interaction terms AB and AC were also insignificant ($p>0.05$). As a result, non-significant parameters ($p>0.05$) were eliminated to create the final predictive equation (**Eq. 3.4**), resulting in a streamlined model emphasizing the key factors influencing particle size.

Table 3.8. ANOVA of particle size for quadratic model for high-pressure homogenization

Source	Sum of Squares	df	Mean Square	F-value	p-value	
Model	66452.44	9	7383.60	86.75	< 0.0001	**Significant** ***
A-Pressure	19404.50	1	19404.50	227.98	< 0.0001	***
B-Passes	162.00	1	162.00	1.90	0.2102	
C-Concentration	2888.00	1	2888.00	33.93	0.0006	***
AB	132.25	1	132.25	1.55	0.2527	
AC	110.25	1	110.25	1.30	0.2925	
BC	25440.25	1	25440.25	298.90	< 0.0001	***
A^2	2470.95	1	2470.95	29.03	0.0010	**
B^2	8050.00	1	8050.00	94.58	< 0.0001	***
C^2	8630.84	1	8630.84	101.40	< 0.0001	***
Lack of Fit	469.00	3	156.33	4.93	0.0786	**not significant**
R-squared	**0.9911**					
Adj R-squared	**0.9797**					

*Significant at p<0.1, **Significant at p<0.05, ***Significant at p<0.001, df: degrees of freedom

Particle size = 776.575 - 1.8168 A - 506.65 B + 20.595 C + 0.046 AB + 0.0042 AC + 7.975 BC + 0.0015504 A^2 + 43.725 B^2 - 0.45275 C^2

Eq. 3.4

The determination coefficient (R^2) of 0.9911 indicates that 99.11% of the variation in particle size optimization efficiency was explained by the independent variables, with only 0.89% remaining unexplained by the model. The lack of fit was insignificant relative to pure error (p>0.05), validating the model's reliability. This confirms the model's suitability for effectively optimizing particle size during high-pressure homogenization.

Table 3.9. ANOVA of zeta potential for quadratic model for high-pressure homogenization

Source	Sum of Squares	df	Mean Square	F-value	p-value	
Model	126.34	9	14.04	25.03	0.0002	**Significant** ***
A-Pressure	8.82	1	8.82	15.73	0.0054	**
B-Passes	4.31	1	4.31	7.68	0.0276	**
C-Concentration	8.59	1	8.59	15.32	0.0058	**
AB	2.72	1	2.72	4.86	0.0634	*
AC	0.4225	1	0.4225	0.7534	0.4142	
BC	1.45	1	1.45	2.59	0.1516	
A^2	90.93	1	90.93	162.16	0.0001	***
B^2	9.10	1	9.10	16.23	0.0050	**
C^2	1.67	1	1.67	2.98	0.1281	
Lack of Fit	1.79	3	0.5965	1.12	0.4409	**not significant**
R-squared	**0.9699**					
Adj R-squared	**0.9311**					

*Significant at p<0.1, **Significant at p<0.05, ***Significant at p<0.001, df: degrees of freedom

The ANOVA table for zeta potential (**Table 3.9**) showed a significant model fit (p<0.0002). While the linear parameters pressure, passes and concentration were significant (p<0.05). Interaction terms AB, AC and BC were insignificant (p>0.05). As a result, the final predictive equation (**Eq. 3.5**) was formulated by omitting non-significant parameters (p>0.05), yielding a streamlined model focused on the critical variable influencing zeta potential.

Zeta potential = $-9.198 + 1.05\ A + 0.73375\ B + 1.03625\ C - 0.825\ AB - 0.325\ AC - 0.6025\ BC - 4.64725\ A^2 + 1.47025\ B^2 - 0.62975\ C^2$ **Eq. 3.5**

The determination coefficient (R^2) of 0.9699 indicates that 96.99% of the variation in zeta potential optimization efficiency was explained by the independent variables, with 3.01%

unexplained by the model. The lack of fit was insignificant relative to pure error ($p>0.05$), validating the model's accuracy. This confirms the model's reliability for optimizing zeta potential during high-pressure homogenisation, ensuring robust performance in predicting outcomes.

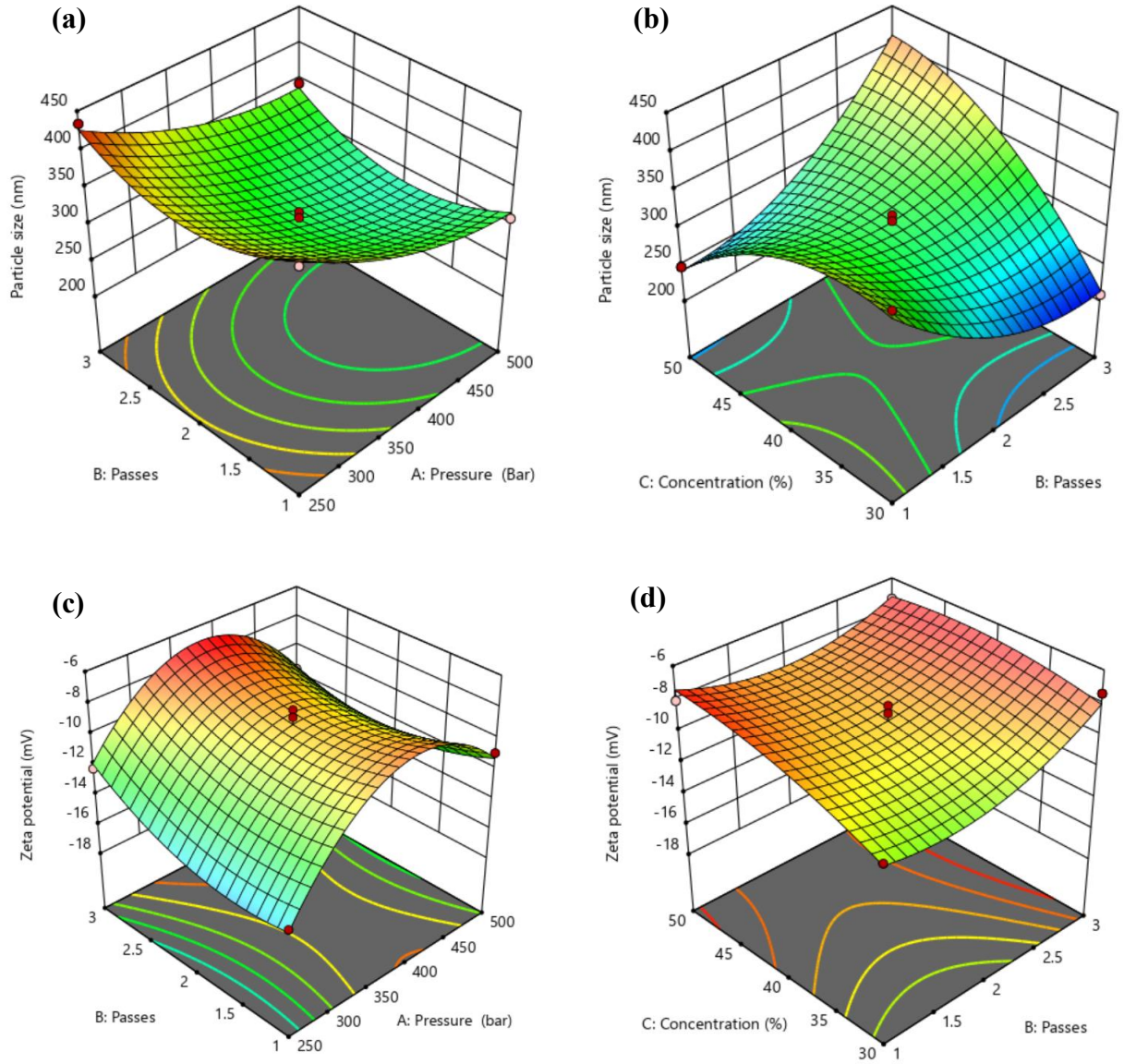

Fig. 3.5. 3D surface graphs of (a, b) particle size and (c, d) zeta potential of nanocellulose obtained by high-pressure homogenization.

Through the use of three-dimensional response surface profiles produced by various non-linear regression models, the interactive effects of independent factors on particle size and

zeta potential were assessed. The independent variables viz., pressure, passes, and concentration were plotted on the z-axis to create 3D surface and contour graphs, providing insight into their effects on the dependent variables. **Fig 3.5** illustrates the interactions between pressure, passes, and concentration on particle size and zeta potential. In the graph particle size initially decreased with lower passes and pressure, followed by a reverse trend as these parameters increased. Additionally, particle size was observed to increase with decreasing passes. For zeta potential, an increase was observed with higher passes and pressure, though a reverse trend emerged at certain levels. Interestingly, zeta potential initially decreased with increasing concentration but then increased beyond a certain threshold. The interaction between passes and pressure exhibited a negative effect, indicating that higher passes and pressure led to a decrease in particle size. Conversely, the interaction between concentration and passes demonstrated a positive effect, signifying that increased concentration and passes resulted in larger particle size. These findings suggest that passes play a critical role in optimizing particle size. For zeta potential, the interaction between passes and pressure showed a positive effect, indicating that higher passes and pressure increased zeta potential. However, the interaction between concentration and passes displayed a negative effect, revealing that higher concentration and passes caused a decrease in zeta potential. Collectively, these results emphasize the importance of passes in optimizing both particle size and zeta potential.

Table 3.10. Optimum conditions, experimental and predicted value obtained for high-pressure homogenization

Optimum Conditions	Coded Levels	Actual Levels	
Pressure (bar)	1.00	500	
Passes	-0.206	2	
Concentration (%)	-1.00	30	
Response	Predicted Values	Experimental Values	Desirability
Particle size (nm)	328.9	**338.7**	1.00
Zeta potential (mV)	-10.9	**-10.5**	

$$\mathbf{Z=(Z_0-Z_c)/\Delta Z}$$

Where, Z and Z_0 indicate coded and actual levels of independent variables, respectively. ΔZ represents step change while Z_c indicated actual value at central point.

Desirability analysis (**Table 3.10**) validated the process, achieving a maximum desirability score of 1 under optimal conditions of 500 bar pressure, 2 passes, and 30% concentration.

Predicted values for particle size and zeta potential were 328.9 nm and -10.9 mV, respectively, while experimental results were 338.7 nm for particle size and -10.5 mV for zeta potential. The close alignment between predicted and experimental outcomes, corroborated by DLS data (**Fig. 3.6**), demonstrated minimal deviation. These results confirm the reliability of the optimized conditions of high-pressure homogenization for further studies and practical applications in nanocellulose production.

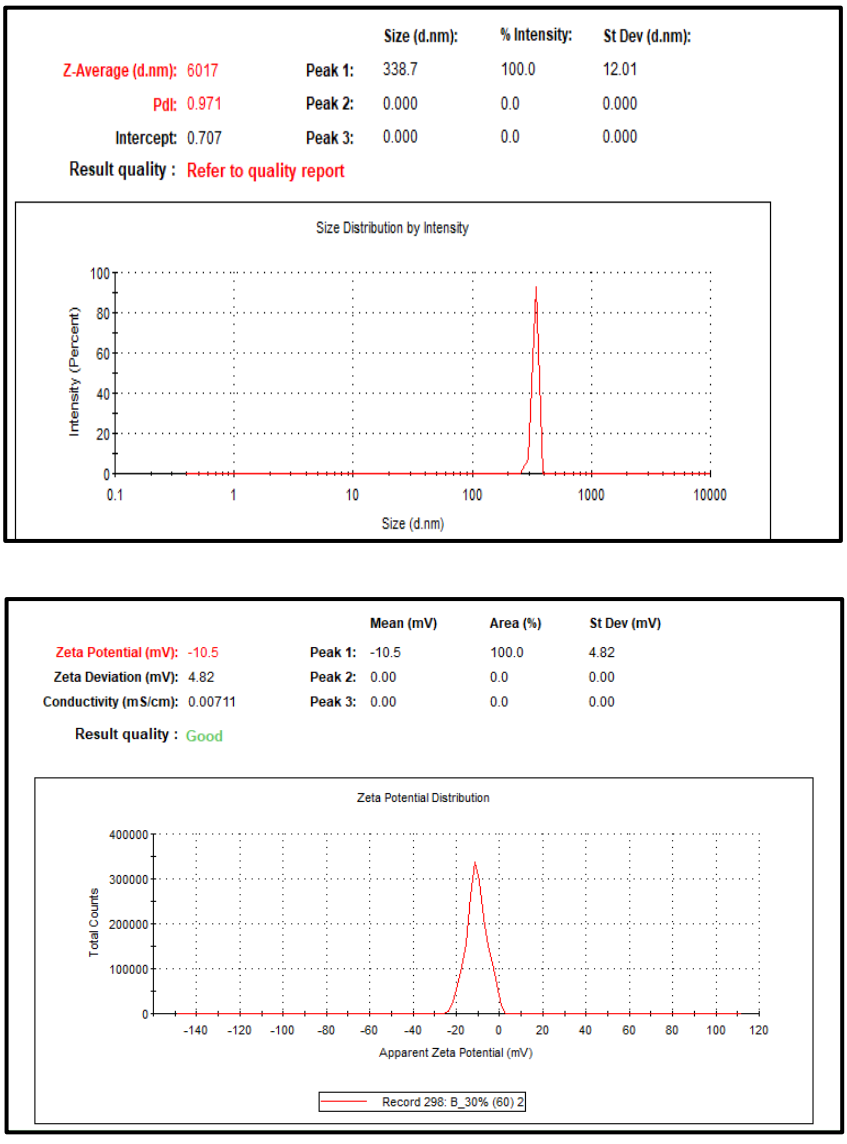

Fig. 3.6. Particle size distribution and zeta potential of the nanocellulose obtained by high pressure homogenization.

3.3.4. Characterisation of nanocellulose obtained from banana rachis

3.3.4.1. Comparative analysis of the morphology of nanocellulose obtained by ultrasonication and high-pressure homogenization

Fig. 3.7 presents a detailed analysis of nanocellulose derived from banana rachis through various stages of processing and characterization. **Fig. 3.7a** shows the nanocellulose suspension, highlighting its uniform and stable dispersion. The translucent or milky appearance, characteristic of nanocellulose, confirms its nanoscale dimensions and high surface area. This visual indicates successful isolation after chemical and mechanical processing, with effective removal of non-cellulosic components and proper stabilization in the medium. **Fig. 3.7b** depicts the freeze-dried nanocellulose sample with a porous, lightweight structure. The freeze-drying process effectively removes moisture, preserving the nanoscale morphology and enhancing the sample's stability for storage and applications. **Fig. 3.7c** presents the SEM image of the cellulose sample treated with ultrasonication. The image illustrates morphological changes, such as ruptured surfaces and reduced fiber diameters, resulting from bleaching and acid hydrolysis. The long, narrow fibrils of relatively uniform size reflect the effective removal of non-cellulosic constituents and the transformation of cellulose into nanocellulose. In contrast, **Fig. 3.7d** shows the SEM image of the cellulose sample treated with high-pressure homogenization. The image reveals a rough, non-fibrillar surface lacking organized, thread-like features, likely due to the homogenizer's ineffectiveness in breaking down fibrillar components. Consequently, ultrasonicated cellulose samples were selected for further characterization.

(a)

(b)

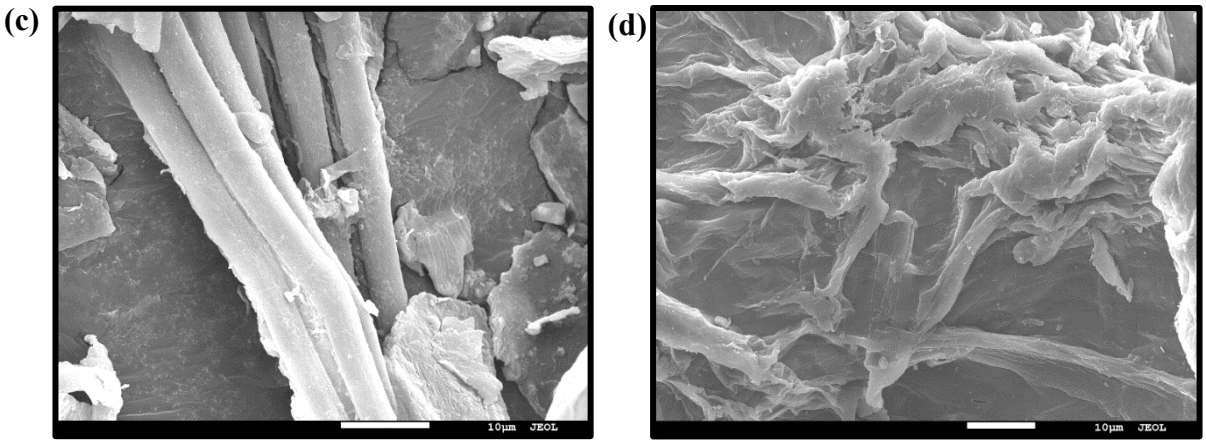

Fig. 3.7. (a) Images of nanocellulose suspension obtained from banana rachis, (b) Freeze dried nanocellulose, (c) SEM images of cellulose obtained from ultrasonication and (d) SEM images of cellulose obtained from high pressure homogenisation.

3.3.4.2. FT-IR spectroscopic analysis of ultrasonicated samples

The FT-IR spectra of the fibre extracted from BR, bleached CF, and NC are shown in **Fig. 3.8**. The large absorption band in the range of 3640–3000 cm^{-1} is due to the –OH stretching vibration seen in primary organic components (cellulose, hemicellulose, and lignin) (Pereira et al., 2014; Fortunati et al., 2016). The peak at 1732 cm^{-1} is brought on by either decreased ester linking of the carboxylic groups of the ferulic and p-coumaric acids of hemicellulose or C=O stretching of the acetyl and uronic ester groups of hemicellulose. (Zuluaga et al., 2009). The –OH group of the absorbed water's bending and stretching vibrations is related to the spectra detected in the region of 1635–1640 cm^{-1} (Fortunati et al., 2016; Rana et al., 2023). The peak at 2916 cm^{-1} is caused by stretching vibrations of the C–H group. The absorption bands at 1027 cm^{-1} are responsible for the interactions between the glucose units in cellulose as well as the C–O–C stretching vibration of the pyranose ring. Additionally, the free O–H stretching vibration of the cellulose molecule's –OH group occurs at the same time as the absorption band in the range of 3500–3350 cm^{-1}. It was evident from the variance in peak intensities between raw BR and NC in the ranges of 2700 to 3600 cm^{-1} and 850 to 1500 cm^{-1} that chemical treatments had an impact on the fibre's chemical composition. Additionally, in the nanocellulose, the transmittance peaks in the range of 850 to 1500 cm^{-1} correlates with the cellulose material's crystal structure decrease. With subsequent treatments, these peaks' height decreased. It is assumed that

the lignin, hemicellulose, and wax were effectively taken out of the fibres during processing.

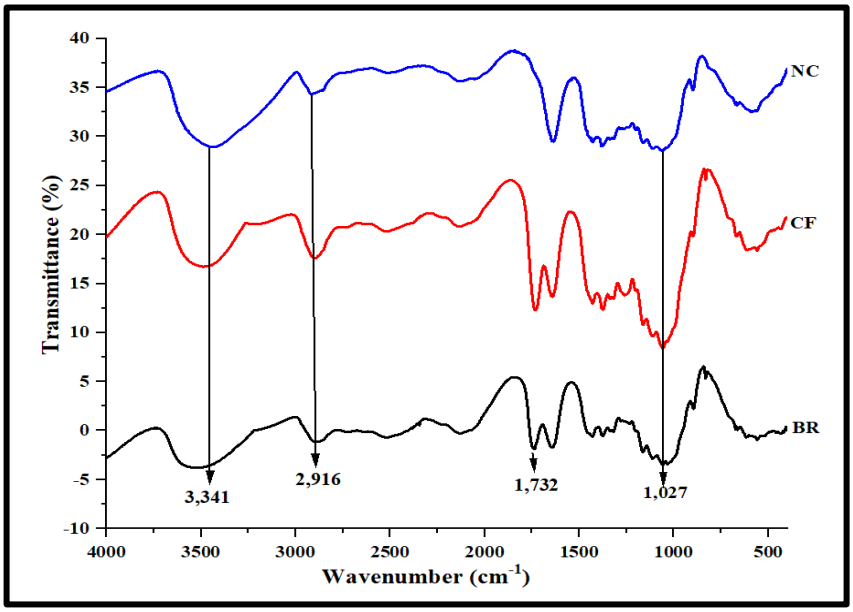

Fig. 3.8. FTIR spectra of powdered banana rachis (BR), cellulose fibre (CF) and nanocellulose (NC) of ultrasonicated samples.

3.3.4.3. XRD analysis of ultrasonicated samples

The powdered XRD pattern in **Fig. 3.9** displays the XRD patterns presented by BR, CF, and NC. The relative crystallinity (RC) and 2θ values for BR, CF, and NC are shown in **Table 3.11**. BR shows two peaks, whereas CF and NC show three peaks. As cellulose nanocrystals were produced rather than cellulose nanofibrils because of alkali treatment and acid hydrolysis, the difference in the crystallinity index between the two processes was small (Hamad et al., 2020). RC values of both CF and NC were higher than their corresponding source material (**Table 3.11**), as previously stated in the FT-IR data, this may be attributed to isolation techniques that largely removed the lignin (**Fig. 3.9**). According to various studies, lignin removal encourages a growth in the material's crystallinity because it is an amorphous substance (de Oliveira et al., 2017; Abraham et al., 2013). Removal of lignin, hemicellulose, and amorphous non- cellulosic compounds during the pre-treatment and bleaching processes improves the crystallinity because they have a negative effect on crystallinity due to the Van der Waals forces and bonding contacts between near molecules and the crystalline structure of saccharide (Faraj et al., 2022).

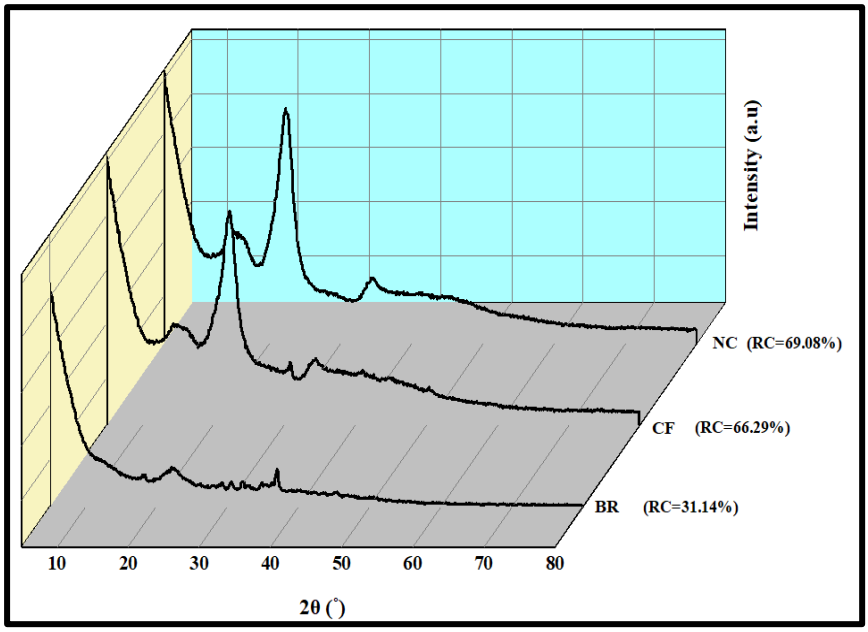

Fig. 3.9. Overlaid powdered X-ray diffraction of ultrasonicated samples. BR, banana rachis; CF, cellulose fibre; and NC, nanocellulose.

Table 3.11. Relative crystallinity and 2θ value of banana rachis, its cellulose fibre and nanocellulose

Material	Relative Crystallinity (%)	2θ (°)
BR	31.14	22.46, 36.84
CF	66.29	14.38, 22.26, 34. 54
NC	69.08	14.88, 22.17, 34.44

BR: Banana rachis; CF: Cellulose fibre; NC: Nanocellulose

3.3.4.4. Thermogravimetric analysis (TGA) and 1st order derivatives (DTG)

The thermal properties of BR, CF, and NC were investigated to analyse the thermal breakdown temperatures and determine the material's thermal behaviour from thermogravimetric analysis (**Fig. 3.10**). The specific order of physical transitions and chemical reactions that take place over predetermined temperature ranges gives rise to thermogravimetric curves, which are distinctive to a given compound or material. At high temperatures, weight changes resulting from the formation and breakdown of physical and chemical bonds are seen (Brown et al., 2003). After the chemical treatment using acid hydrolysis, the thermal stability of the powdered NC was improved, indicating higher

crystallinity. A greater degradation temperature is necessary for crystals with higher crystallinity (Ouajai & Shanks, 2005). It has been reported that the non-cellulose component appears to have a significant influence on the thermal breakdown of the fibres (Kaushik & Singh, 2011). Analyses were performed on the powdered BR, CF, and NC samples, each of which initially weighed 3.36 mg, 9.31 mg, and 1.12 mg, respectively. The curve for weight loss for BR revealed a mild effect; however, CF lost most of its weight at 330°C and 310°C. As shown in **Fig. 3.10**, NC had lost the maximum weight. Due to degradation of cellulosic material by acid hydrolysis and the addition of a sulphate group to the polymer's amorphous region, thermal stability had substantially decreased in NC, and the results are in concurrence with Moreno et al. (2018). The steepness of the NC curve determines the phase purity and the quality of the NC (Mandal & Chakrabarty, 2011).

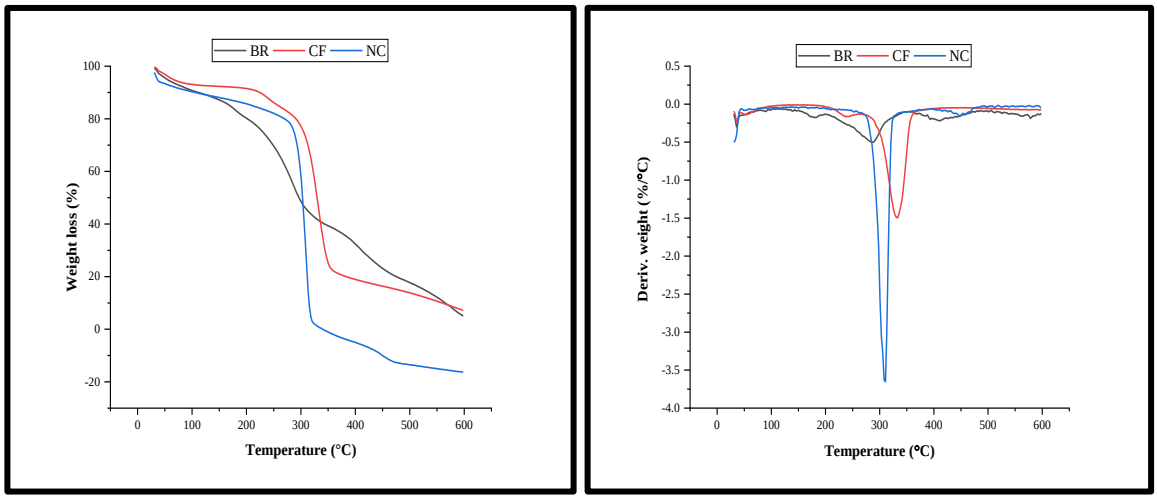

Fig. 3.10. TGA, and DTG curve of samples. BR, banana rachis; CF, cellulose fibre; and NC, nanocellulose.

3.3.4.5. Differential scanning calorimetry (DSC) of ultrasonicated samples

The heating DSC curves for banana rachis powder, cellulose fibre and nanocellulose are expressed in terms of heat flow (**Fig. 3.11a-c**). The results of DSC analysis are presented in **Table 3.12**. The initial endothermic peak suggests the evaporation of moisture or volatile components, typical for materials with bound water or solvents. The subsequent exothermic peaks indicate thermal degradation or decomposition of organic components, highlighting the material's thermal stability and breakdown behaviour at higher temperature. Thermal analysis from **Fig. 3.11a** reveals distinct thermal behaviour stages.

The first endothermic peak between 46.4°C and 83.0°C corresponds to the removal of bound water or moisture, with a heat absorption of 79.09 J/g. The following exothermic peaks at 291.9°C–304.2°C and 389.0°C–392.0°C suggest partial decomposition and secondary degradation, releasing 16.77 J/g and -8.973 J/g, respectively. **Fig. 3.11b** shows an endothermic peak at 90.8°C, reflecting moisture evaporation with an energy absorption of 181.9 J/g. The exothermic peak at 332.1°C indicates decomposition or structural changes, releasing 43.7 J/g. The first endothermic peak generally reflects the release of low-temperature volatiles or moisture, while the second exothermic peak marks the decomposition temperature, providing insight into the material's thermal stability. In **Fig. 3.11c**, the endothermic peak at 84.3°C corresponds to moisture removal (165.7 J/g), while the exothermic peak at 312.1°C indicates thermal degradation, releasing 100.7 J/g.

The enthalpy values for the breakdown of cellulose, hemicellulose, and moisture desorption, as presented in **Table 3.12**, reveal that nanocellulose (NC) exhibits higher enthalpy values than banana rachis powder. Among the samples, banana rachis powder has the lowest enthalpy values, while NC demonstrates the highest. This increase in enthalpy is attributed to the chemical treatments - alkaline, bleaching, and acid treatments, which enhance the crystalline cellulose content and yield NC. By strengthening the hydrogen bonds between the densely packed cellulose chains and raising the fibres' percentage crystallinity, these treatments stabilise the structure and raise enthalpy values (Deepa et al., 2015). The results show that when each processing stage is completed, the fibres' thermal stability increases, reaching its peak in nanocellulose after acid treatment. The results of the DSC and TGA tests verify that the isolated nanocellulose has excellent thermal characteristics, making it less susceptible to degradation and suitable for processing at elevated temperatures compared to untreated materials.

Table 3.12. Thermal parameters of raw and treated banana rachis obtained from DSC analysis

Samples	Onset temperature (°C)	Peak temperature (°C)	Enthalpy of degradation (ΔH) (J/g)
Banana rachis	46.4	83.0 (endo)	79.09
	291.9	304.2 (exo)	16.77
	389.0	392.0 (endo)	8.973
Cellulose fibre	56.3	90.8 (endo)	181.9
	324.2	332.1 (endo)	43.7
Nanocellulose	50.1	83.3 (endo)	165.7
	321.5	312.1 (endo)	100.7

(a)

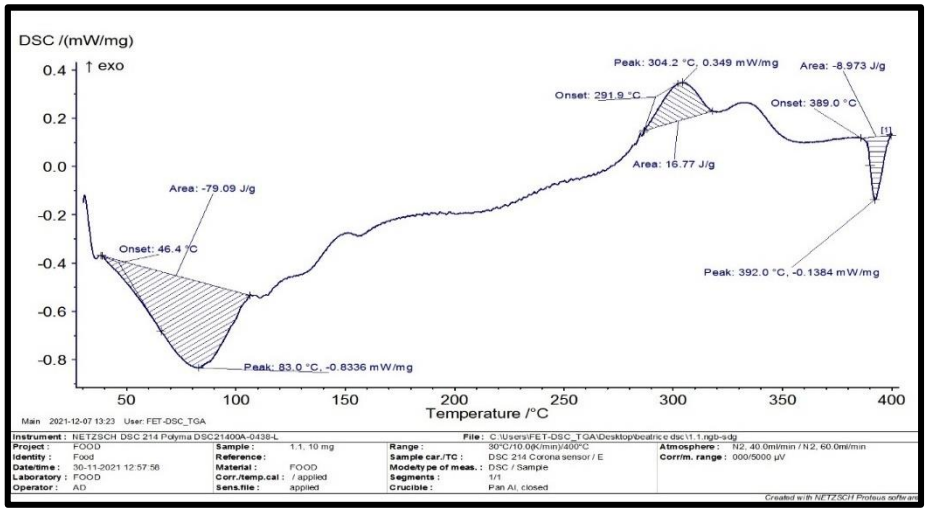

(b)

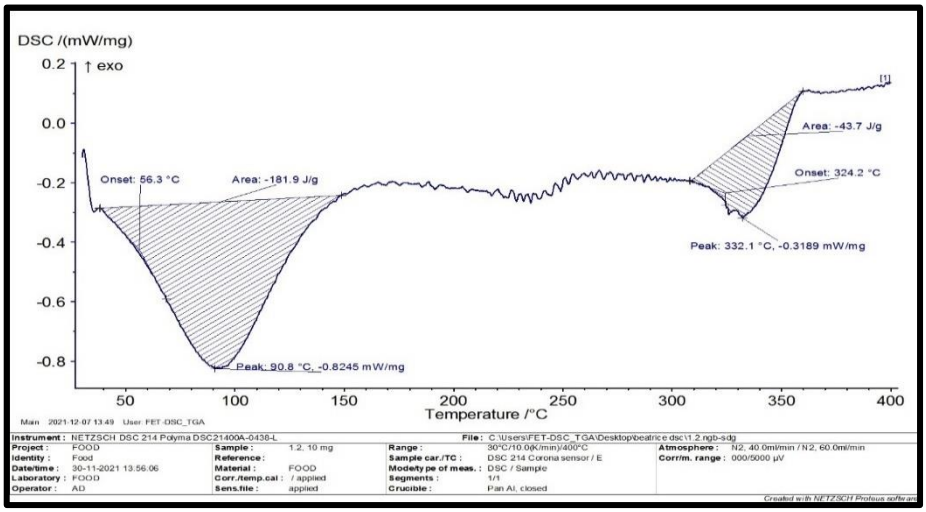

(c)

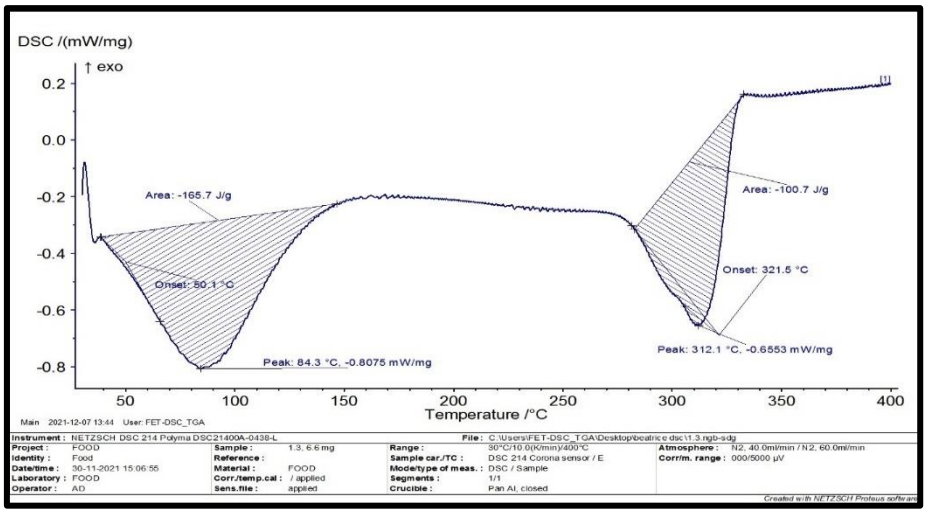

Fig. 3.11. DSC curve of (a) banana rachis powder, (b) cellulose fibre, and (c) nanocellulose.

3.3.4.6. Morphological analysis of nanocellulose obtained by ultrasonication

In **Fig. 3.12**, the FE-SEM images of BR, CF, and NC are compared for 10µm (**Fig. 3.12a, b, and c**) and 1µm (**Fig. 3.12x, y, and z**) scale. Owing to the existence of an external non-cellulosic layer made up of cementing agents such pectin, lignin, hemicelluloses, wax, and oil, as shown in **Fig. 3.12a**, the surface of BR appeared to be smooth, and a clearer view was observed in **Fig. 3.12x**. **Fig. 3.12b and y** display pictures of irregular surface, and the figure clearly illustrates how the fibre bundles were separated into microscopic, individual fibres in bleached CF. The FT-IR investigation determined that the main cause of this observation was the elimination of lignin and hemicelluloses, as well as a few other extractives, during the chemical treatments. Images of the oven-dried, acid-hydrolysed NC are presented in **Fig. 3.12c and z**. NC tends to self-assemble into fibres that are less than a micron broad and a micrometre long after drying. This might be because as CF dries, the surface hydroxyl groups become more strongly attracted to one another through hydrogen bonding (Jiang & Hsieh, 2013). After acid hydrolysis, fibre samples showed a decrease in fibre diameter because of the successful removal of the amorphous phase, as shown by particle size analysis. After mechanical agitation and acid hydrolysis, the fibres had successfully undergone nano-scale individualization. Effective acid hydrolysis resulted in the production of NC with rod- shaped and rectangular structures (Deepa et al., 2015).

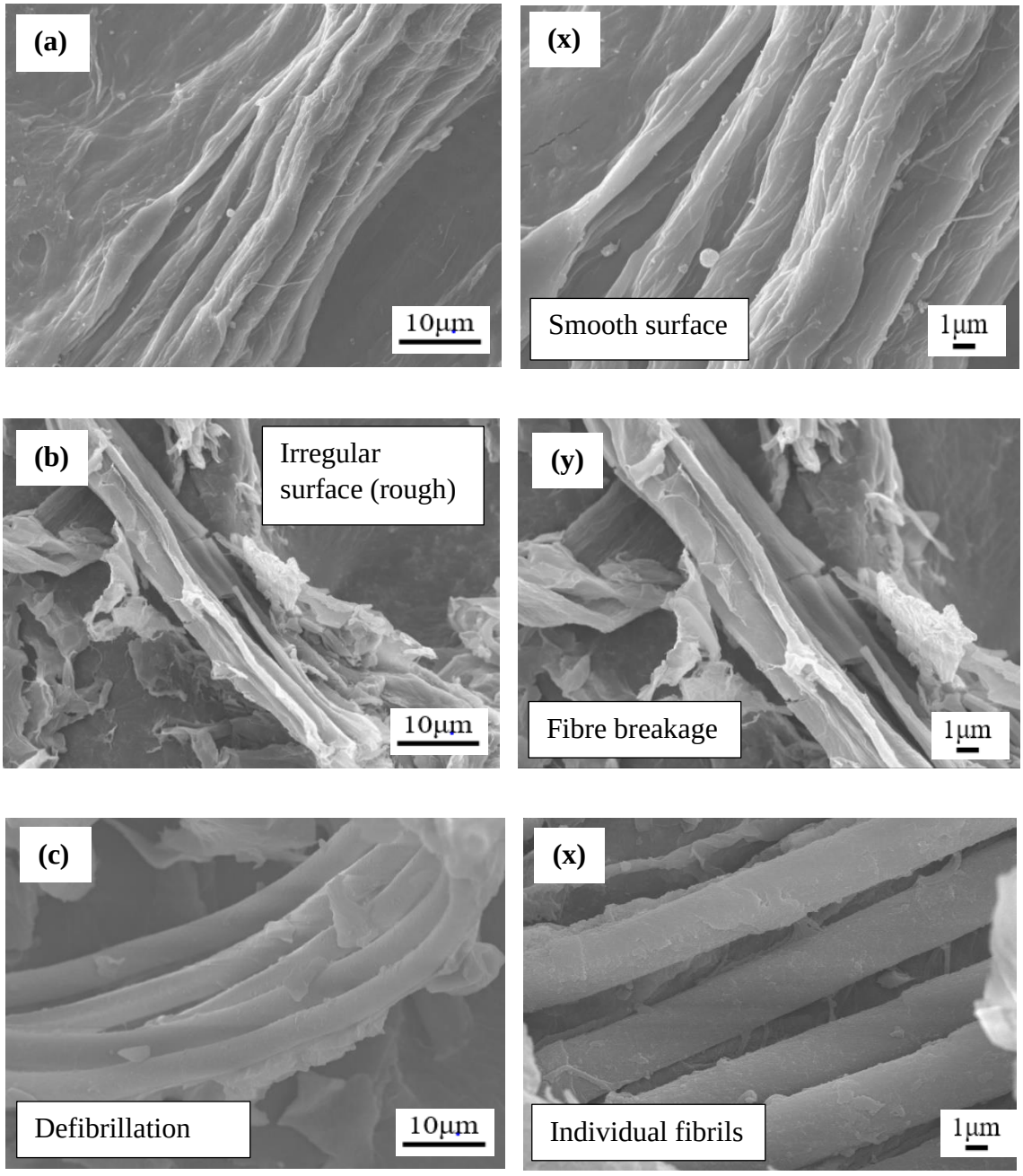

Fig. 3.12. FE-SEM micrographs of the BR, CF, and NC for 10 µm (a, b, and c) and 1 µm (x, y, and z) scale, respectively.

3.3.4.7. TEM analysis of ultrasonicated nanocellulose samples

Analysing the morphology of nanocellulose is essential, as the cellulose source and hydrolysis technique significantly influence its dimensions and properties. To examine the size and shape of nanocellulose samples, TEM examinations were performed, with results shown in **Fig. 3.13.** The diameter of nanocellulose was within the nanometer range,

confirming the successful extraction of cellulose nanofibrils from banana rachis. The TEM images revealed individualized, rod-like nanofibrils, demonstrating the efficiency of acid hydrolysis in isolating nanocellulose. These results are consistent with earlier research by Abraham et al. (2011), Kaushik and Singh (2011), Xu et al. (2013), Wang et al. (2012), and Sacui et al. (2014). The exact length of the nanofibrils could not be measured accurately due to their bundled and overlapping appearance, likely caused by interfibrillar hydrogen bonding. However, the images suggest that the nanofibrils are few nanometers long, resulting in a high aspect ratio (length-to-diameter ratio). The aspect ratio is a critical parameter for processing composites with enhanced mechanical properties. Higher aspect ratios improve composite strength and performance, even at low nanocellulose concentrations, as noted by Faria et al. (2015). These observations highlight the potential of nanocellulose for applications requiring strong and lightweight composite materials.

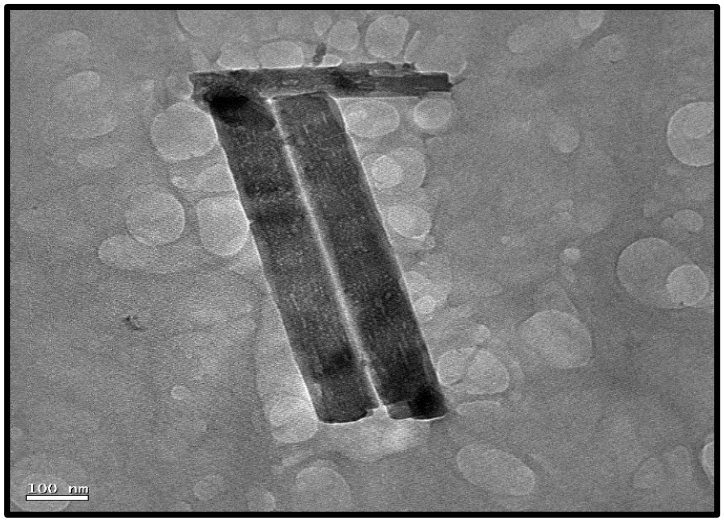

Fig. 3.13. TEM micrograph of the nanocellulose (NC).

3.3.4.8. AFM analysis of ultrasonicated nanocellulose samples

Morphological examination of nanocellulose is critical as the cellulose source and hydrolysis technique significantly influence its dimensions and properties. To assess the morphology and size of nanocellulose samples obtained from banana rachis, AFM analyses were conducted, and the topography images are presented in **Fig. 3.14.** The AFM images demonstrate the effective isolation of nanocellulose from microsized fibers, highlighting the successful breakdown into nanoscale fibrils. Nanocellulose samples from different sources exhibited a rod-like, nanofibrillar network structure, with some degree of aggregation (Guerra et al., 2021). The overlapping and bundling of individual cellulose

nanofibrils due to intermolecular interactions, such as hydrogen bonding, complicate the precise measurement of fibril size and aspect ratio through the AFM technique. Despite this limitation, the AFM results confirm the nanoscale dimensions of the fibrils and their aggregation tendency, which could influence the performance of nanocellulose in applications such as composite materials and nanotechnology-based systems.

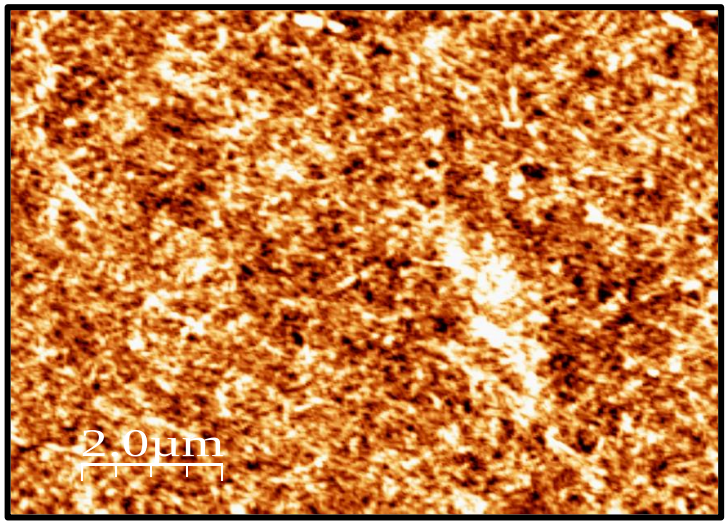

Fig. 3.14. AFM image of the nanocellulose.

3.3.5. Isolation of nanocellulose from pineapple peel

The process of isolating nanocellulose (NC) from pineapple peel is depicted in **Fig. 3.15**. Chemical reagents were utilized to eliminate non-cellulosic components from the fibers. The process began with treating the fibers using a hexane-ethanol mixture to swell the fibers, enhancing reagent penetration. Next, sodium hydroxide was applied to remove hemicellulose and improve the solubility of both lignin and hemicellulose. The fibers were then bleached using a mixture of acetic acid and nitric acid, resulting in cellulose fibers referred to as bleached fibers. These bleached fibers underwent hydrolysis with sulfuric acid, which esterified the hydroxyl groups and reduced the particle size (Moreno et al., 2018). The resulting nanocellulose was washed repeatedly to achieve a neutral pH and subsequently sonicated in an ice bath to produce rod-shaped nanocellulose. This systematic chemical treatment effectively isolated high-quality rod-shaped nanocellulose by removing non-cellulosic components and refining the cellulose structure.

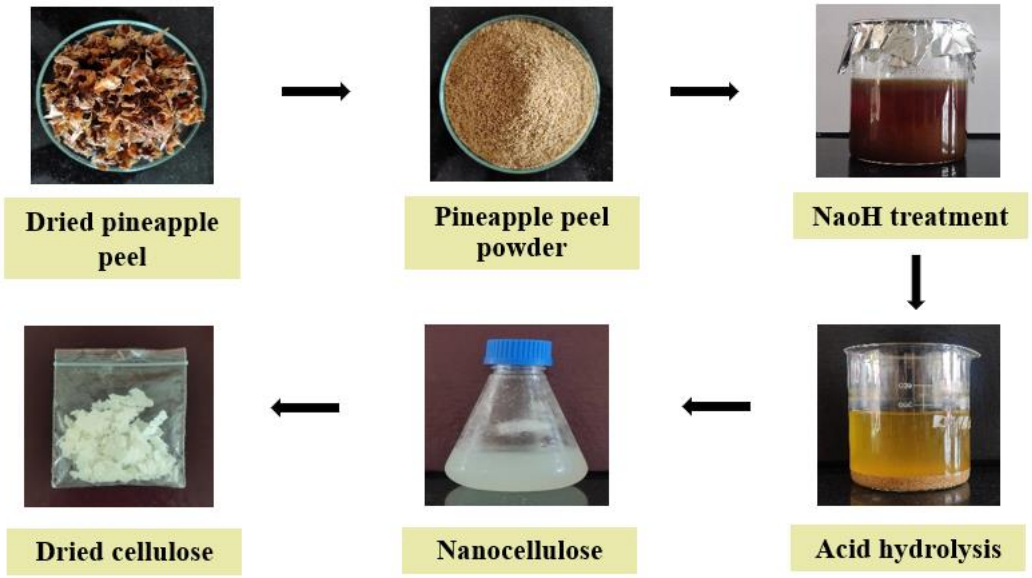

Fig. 3.15. Stages of treatment during nanocellulose isolation from pineapple peel.

3.3.6. Modelling and fitting using ultrasonication (US) for pineapple peel

The effects of time, temperature, and concentration on particle size and zeta potential were studied using response surface methodology. Design-Expert software facilitated regression analysis to fit a second-order quadratic polynomial based on Box-Behnken Design. Analysis of variance determined regression coefficients for linear, quadratic, and interaction terms. These coefficients were utilized to generate 3D surface and contour plots, visualizing relationships between responses and experimental factor levels. This approach also enabled the determination of optimal conditions. Experimental data and responses obtained from the Box-Behnken Design are summarized in **Table 3.13**.

Table 3.13. Particle size and zeta potential obtained for the independent variables using ultrasonication

Run	Independent Variables			Response	
	Time (min)	Temperature (°C)	Concentration (%)	Particle size (nm)	Zeta potential (mV)
1	40	60	25	123	-20.2
2	40	50	35	114	-9.8
3	60	50	45	74	-8.2
4	20	50	25	158	-13.8
5	20	60	35	102	-16.7
6	20	40	35	196	-6.1
7	40	60	45	86	-6.6
8	40	40	25	138	-6.2
9	40	50	35	125	-7.1
10	40	50	35	120	-7.6
11	20	50	45	104	-7.2
12	40	50	35	132	-7.9
13	60	40	35	75	-12.2
14	40	40	45	128	-12
15	60	50	25	78	-14.6
16	40	50	35	133	-8.2
17	60	60	35	108	-11.8

The ANOVA table for particle size (**Table 3.14**) showed a significant model fit ($p<0.0001$). While all the linear parameters time, temperature and concentration were found to be significant ($p<0.001$). It was determined that the interaction terms AC and BC were not significant ($p>0.001$). Consequently, non-significant parameters ($p>0.05$) were eliminated in the formulation of the final prediction equation (**Eq. 3.6**), yielding a streamlined model focused on the critical variable influencing particle size.

Particle size = $542.112 - 9.55125\,A - 10.8125\,B + 7.5425\,C + 0.15875\,AB + 0.0625\,AC - 0.0675\,BC - 0.02475\,A^2 + 0.0535\,B^2 - 0.114\,C^2$ **Eq. 3.6**

Table 3.14. ANOVA of particle size for quadratic model obtained for ultrasonication

Source	**Sum of Squares**	**df**	**Mean Square**	**F-value**	**p-value**	
Model	15372.48	9	1708.05	42.85	< 0.0001	**Significant** ***
A-Time	6328.12	1	6328.12	158.74	< 0.0001	***
B-Temperature	1740.50	1	1740.50	43.66	0.0003	***
C-Concentration	1378.13	1	1378.13	34.57	0.0006	***
AB	4032.25	1	4032.25	101.15	< 0.0001	***
AC	625.00	1	625.00	15.68	0.0055	**
BC	182.25	1	182.25	4.57	0.0698	*
A^2	412.67	1	412.67	10.35	0.0147	*
B^2	120.52	1	120.52	3.02	0.1256	
C^2	547.20	1	547.20	13.73	0.0076	**
Lack of Fit	20.25	3	6.75	0.1043	0.9533	**not significant**
R-squared	**0.9822**					
Adj R-squared	**0.9592**					

*Significant at p<0.1, **Significant at p<0.05, ***Significant at p<0.001, df: degrees of freedom

As indicated by the determination coefficient (R^2) of 0.9822, 98.22% of the sample changes for the particle size optimisation efficiency were linked to the independent variables, whereas the model was unable to explain 1.78% of the total variations. The model has been tested and may work well for optimising particle size for ultrasonication, as evidenced by the lack of fit being found to be negligible equivalent to pure error (p>0.05).

Table 3.15. ANOVA of zeta potential for quadratic model obtained for ultrasonication

Source	Sum of Squares	df	Mean Square	F-value	p-value	
Model	260.57	9	28.95	25.55	0.0002	**Significant** ***
A-Time	1.13	1	1.13	0.9927	0.3523	
B-Temperature	44.18	1	44.18	38.98	0.0004	***
C-Concentration	54.08	1	54.08	47.72	0.0002	***
AB	30.25	1	30.25	26.69	0.0013	**
AC	0.0100	1	0.0100	0.0088	0.9278	
BC	94.09	1	94.09	83.02	< 0.0001	***
A^2	11.32	1	11.32	9.99	0.0159	**
B^2	15.85	1	15.85	13.98	0.0073	**
C^2	5.96	1	5.96	5.26	0.0555	**
Lack of Fit	3.75	3	1.25	1.19	0.4188	**not significant**
R-squared	**0.9705**					
Adj R-squared	**0.9325**					

*Significant at p<0.1, **Significant at p<0.05, ***Significant at p<0.001, df: degrees of freedom

The ANOVA table for zeta potential (**Table 3.15**) showed a significant model fit (p<0.0002). While the linear parameters temperature and concentration were significant (p<0.05), time was insignificant (p>0.05). Interaction terms AB and AC were also insignificant (p>0.001). As a result, the final predictive equation (**Eq. 3.7**) was formulated by omitting non-significant parameters (p>0.05), yielding a streamlined model focused on the critical variable influencing zeta potential.

Zeta potential = $37.6675 - 0.3695\ A - 0.5425\ B - 1.322\ C + 0.01375\ AB - 0.00025\ AC + 0.0485\ BC - 0.0041\ A^2 - 0.0194\ B^2 - 0.0119\ C^2$ **Eq. 3.7**

The determination coefficient (R^2) of 0.9705 indicates that 97.05% of the variation in zeta potential optimization efficiency was explained by the independent variables, with 2.95%

unexplained by the model. The lack of fit was insignificant relative to pure error ($p>0.05$), validating the model's accuracy. This confirms the model's reliability for optimizing zeta potential during ultrasonication, ensuring robust performance in predicting outcomes.

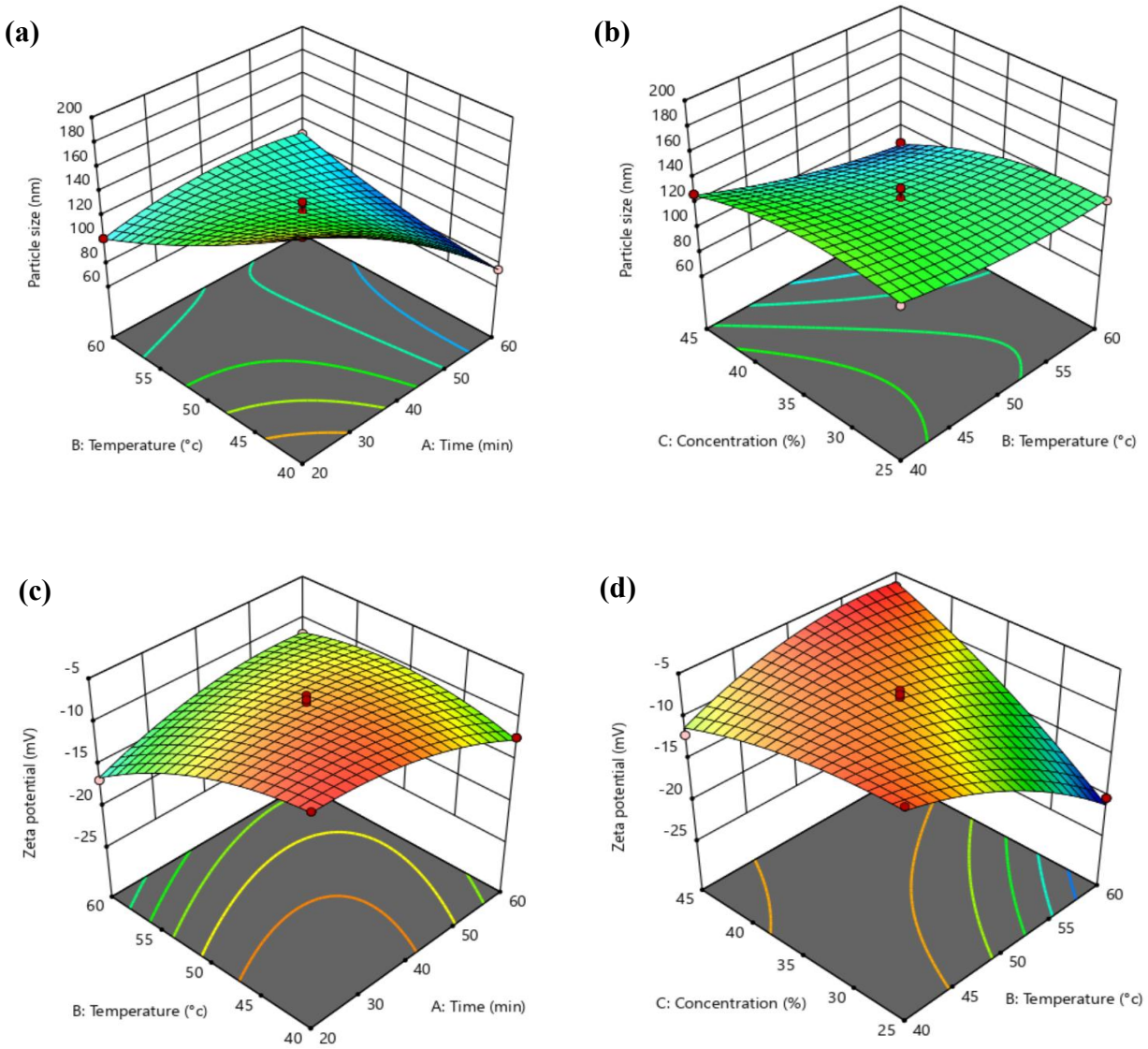

Fig. 3.16. 3D surface graphs of (a, b) particle size and (c, d) zeta potential of nanocellulose obtained by ultrasonication.

Three-dimensional response surface profiles obtained from non-linear regression models were used to assess the combined effects of temperature, concentration, and time on particle size and zeta potential. Independent variables were plotted on the z-axis to generate 3D surface and contour graphs, offering insights into their influence on the

dependent variables. **Fig. 3.16** illustrates these interactions. For particle size, an initial increase was observed with rising time and temperature, followed by a slight reversal after reaching a threshold. Conversely, particle size decreased consistently with higher concentrations, showing no reversal. For zeta potential, an increase was observed with rising time, temperature, and concentration, without any subsequent decline. The interaction between time and temperature showed a positive effect on particle size, indicating that their simultaneous increase caused particle size to rise. In contrast, the interaction between temperature and concentration exhibited a negative trend, suggesting that higher concentrations combined with elevated temperatures reduced particle size. These findings underscore temperature as a critical factor for optimizing particle size. For zeta potential, the interaction between time and temperature displayed a positive effect, with their combined increase enhancing zeta potential. Similarly, the interaction between concentration and temperature demonstrated a positive impact, as higher levels of both variables led to increased zeta potential. Overall, temperature emerged as a key determinant influencing both particle size and zeta potential. These results provide valuable insights for optimizing process conditions to achieve the desired outcomes during the experimental optimization process.

Table 3.16. Optimum conditions, experimental and predicted values obtained for ultrasonication

Optimum Conditions	Coded Levels	Actual Levels	
Time (min)	-1.00	20	
Temperature (°C)	-1.00	40	
Concentration (%)	-1.00	25	
Response	Predicted Values	Experimental Values	Desirability
Particle size (nm)	181.31	**196.20**	1.00
Zeta potential (mV)	-5.67	**-8.26**	

$$\mathbf{Z=(Z_0-Z_c)/\Delta Z}$$

Where, Z and Z_0 indicate coded and actual levels of independent variables, respectively. ΔZ represents step change while Z_c indicated actual value at central point.

The process was validated using desirability analysis (**Table 3.16**), achieving the highest desirability score of 1 under optimal conditions: time of 20 min, temperature of 40 °C, and

concentration of 25%. The predicted particle size and zeta potential were 181.31 nm and -5.67 mV, respectively, while experimental results were 196.20 nm for particle size and -8.26 mV for zeta potential. The close agreement between predicted and experimental values, supported by DLS data (**Fig. 3.17**), demonstrated minimal deviation. These findings confirm the validity of the optimized conditions for synthesizing nanocellulose from pineapple peel, ensuring their reliability for further study and application in nanocellulose production.

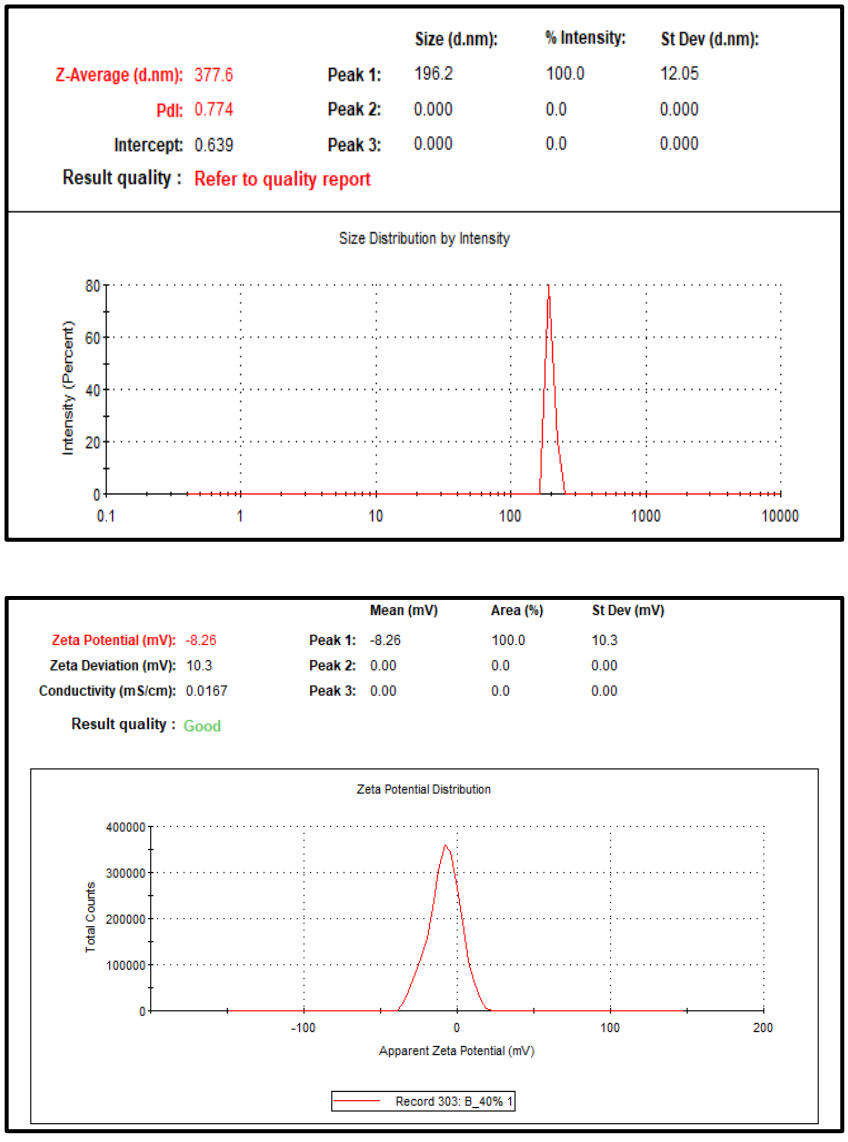

Fig. 3.17. Particle size distribution and zeta potential of the nanocellulose obtained by ultrasonication.

3.3.7. Modelling and fitting using high-pressure homogenisation (HPH) for pineapple peel

The influence of pressure, passes, and concentration on particle size and zeta potential was analysed using response surface methodology. Design-Expert software was employed for regression analysis, fitting a second-order quadratic equation based on the Box-Behnken Design. Analysis of variance determined regression coefficients for linear, quadratic, and interaction terms. To illustrate relationships between responses and factor levels, 3D surfaces and contour plots were generated from the fitted equation. The experimental design and responses obtained through the Box-Behnken Design, detailed in **Table 3.17**, offer valuable insights into optimizing process conditions for particle size and zeta potential.

Table 3.17. Particle size and zeta potential obtained for the independent variables using ultrasonication

Run	Independent Variables			Response	
	Pressure (Bar)	Passes	Concentration (%)	Particle size (nm)	Zeta potential (mV)
1	375	2	40	311	-7.2
2	250	2	30	319	-12.2
3	375	1	30	364	-10.2
4	375	1	50	241	-8.4
5	250	1	40	412	-16.8
6	375	3	50	398	-6.1
7	375	2	40	308	-8.6
8	500	2	50	257	-6.9
9	250	3	40	424	-13.8
10	375	3	30	201	-7.6
11	500	3	40	339	-11.7
12	375	2	40	298	-8.1
13	375	2	40	310	-8.8
14	250	2	50	363	-10.4
15	500	2	30	204	-9.1
16	375	2	40	321	-8.7
17	500	1	40	302	-13.5

The ANOVA table for particle size (**Table 3.18**) demonstrated a significant model fit ($p < 0.0001$). While pressure and concentration were significant ($p < 0.001$), passes were insignificant ($p > 0.1$). Similarly, interaction terms AB and AC were also insignificant ($p > 0.1$). Accordingly, the final predictive equation (**Eq. 3.8**) was refined by excluding non-significant parameters ($p > 0.05$), yielding a streamlined model focused on the key factors affecting particle size.

Particle size = $686.65 - 1.6536\ A - 483.175\ B + 22.3025\ C + 0.05\ AB + 0.0018\ AC + 8\ BC + 0.0014208\ A^2 + 37.45\ B^2 - 0.4605\ C^2$ **Eq. 3.8**

Table 3.18. ANOVA of particle size for quadratic model obtained for high-pressure homogenization

Source	**Sum of Squares**	**df**	**Mean Square**	**F-value**	**p-value**	
Model	67402.05	9	7489.12	65.70	< 0.0001	**Significant** ***
A-Pressure	21632.00	1	21632.00	189.77	< 0.0001	***
B-Passes	231.13	1	231.13	2.03	0.1975	
C-Concentration	3655.13	1	3655.13	32.06	0.0008	***
AB	156.25	1	156.25	1.37	0.2800	
AC	20.25	1	20.25	0.1776	0.6860	
BC	25600.00	1	25600.00	224.58	< 0.0001	***
A²	2075.12	1	2075.12	18.20	0.0037	**
B²	5905.27	1	5905.27	51.80	0.0002	***
C²	8928.85	1	8928.85	78.33	< 0.0001	***
Lack of Fit	528.75	3	176.25	2.62	0.1876	**not significant**
R-squared	**0.9883**					
Adj R-squared	**0.9733**					

*Significant at p<0.1, **Significant at p<0.05, ***Significant at p<0.001, df: degrees of freedom

The determination coefficient (R^2) of 0.9883 indicates that 98.83% of the variation in particle size optimization was explained by the independent variables, with only 1.17% unexplained. An insignificant lack of fit ($p > 0.05$) validated the model's accuracy. These results confirm the model's reliability and suitability for effectively optimizing particle size during high-pressure homogenization for nanocellulose synthesis from pineapple peel.

Table 3.19. ANOVA of zeta potential for quadratic model obtained for high-pressure homogenization

Source	**Sum of Squares**	**df**	**Mean Square**	**F-value**	**p-value**	
Model	129.15	9	14.35	50.46	< 0.0001	**Significant** ***
A-Pressure	18.00	1	18.00	63.30	< 0.0001	***
B-Passes	11.76	1	11.76	41.36	0.0004	***
C-Concentration	6.66	1	6.66	23.43	0.0019	**
AB	0.3600	1	0.3600	1.27	0.2976	
AC	0.0400	1	0.0400	0.1407	0.7187	
BC	0.0225	1	0.0225	0.0791	0.7866	
A^2	55.25	1	55.25	194.31	< 0.0001	***
B^2	17.65	1	17.65	62.08	0.0001	***
C^2	21.36	1	21.36	75.13	< 0.0001	***
Lack of Fit	0.2425	3	0.0808	0.1850	0.9015	**not significant**
R-squared	**0.9848**					
Adj R-squared	**0.9653**					

*Significant at p<0.1, **Significant at p<0.05, ***Significant at p<0.001, df: degrees of freedom

The ANOVA table for zeta potential (**Table 3.19**) indicated a significant model fit ($p < 0.0001$). Linear parameters viz., pressure, passes, and concentration were significant ($p < 0.1$), while interaction terms (AB, AC, BC) were insignificant ($p > 0.1$). Consequently, the final predictive equation (**Eq. 3.9**) was refined by excluding non-significant parameters (p

> 0.05), resulting in a streamlined model emphasizing the critical variables influencing zeta potential.

Zeta potential = -24.8075 + 0.18748 A + 10.6025 B + -1.72575 C + -0.0024 AB + 8e-05 AC + -0.0075 BC + -0.00023184 A^2 + -2.0475 B^2 + 0.022525 C^2 **Eq. 3.9**

The determination coefficient (R^2) of 0.9848 shows that 98.48% of the variation in zeta potential optimization was explained by the independent variables, with only 1.52% unexplained. An insignificant lack of fit ($p > 0.05$) validated the model's accuracy. These results confirm the model's reliability for optimizing zeta potential during high-pressure homogenization, ensuring robust and precise outcome predictions.

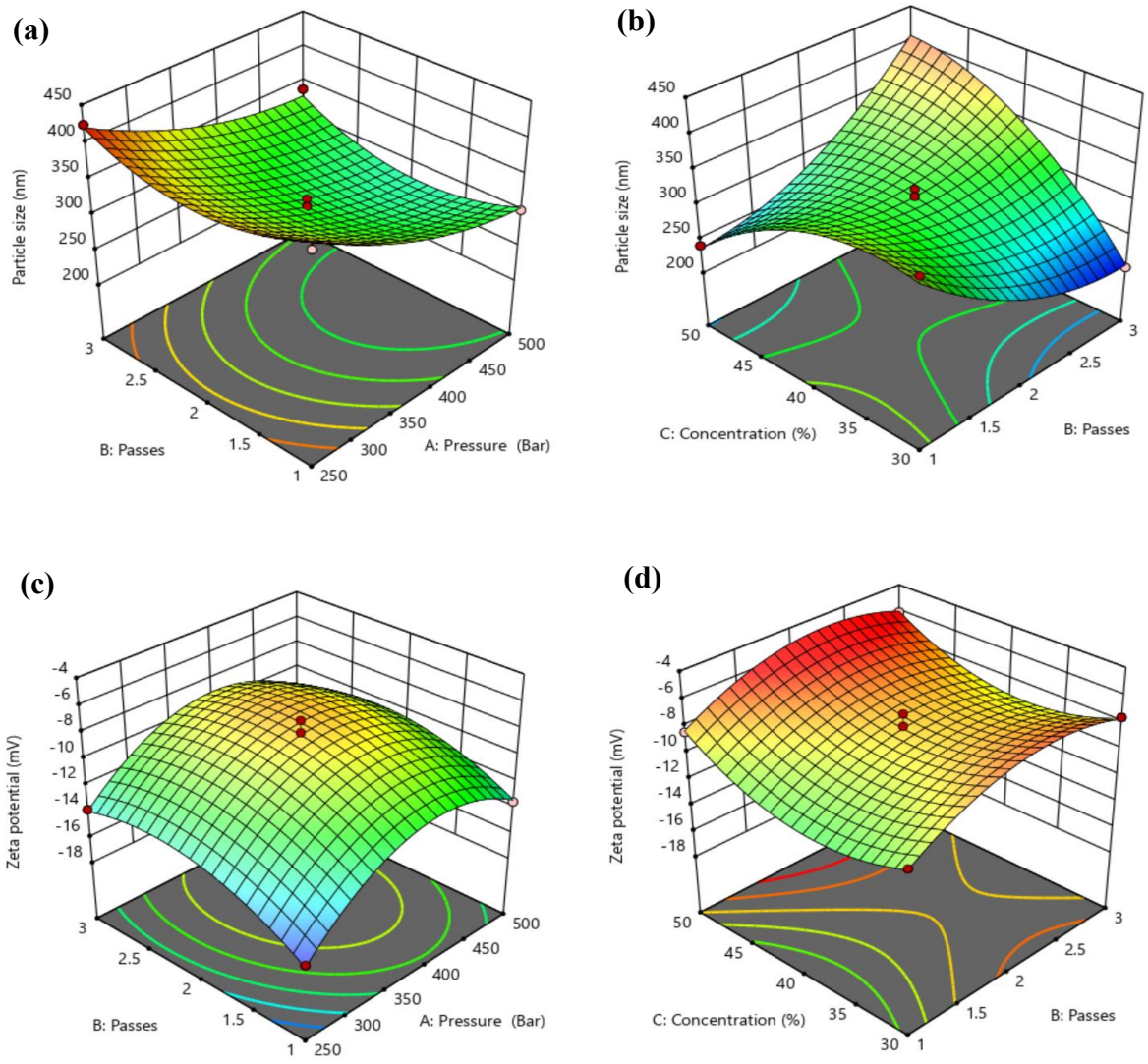

Fig. 3.18. 3D surface graphs of (a, b) particle size and (c, d) zeta potential of nanocellulose obtained by high-pressure homogenization.

Using three-dimensional response surface profiles obtained from non-linear regression models, the combined effects of pressure, passes, and concentration on particle size and zeta potential were examined. These independent variables were plotted along the z-axis to generate 3D surface and contour graphs, providing insights into their influence on the dependent variables. **Fig. 3.18** highlights the interactions between pressure, passes, and concentration. For particle size, an initial decrease was observed with higher passes and pressure, followed by a slight reversal as these parameters continued to increase. Additionally, particle size increased with higher passes and concentration. In the case of zeta potential, it initially increased with higher passes and pressure but reversed at certain levels. Similarly, zeta potential rose with increasing concentration up to a threshold, beyond which it began to decrease. The interaction between passes and pressure had a positive effect on particle size, indicating that higher passes and pressure led to an increase. Similarly, the interaction between concentration and passes showed a positive effect, as higher concentration and passes resulted in larger particle size. For zeta potential, the interaction between passes and pressure was also positive, demonstrating that increasing these variables enhanced zeta potential. The interaction between concentration and passes similarly exhibited a positive effect, with higher concentration and passes increasing zeta potential. The importance of passes in optimising zeta potential and particle size is highlighted by these results. The results also suggest that careful modulation of these parameters is essential for achieving desired outcomes, offering valuable guidance for further optimization in nanocellulose production.

Table 3.20. Optimum conditions, experimental and predicted values obtained for high-pressure homogenization

Optimum Conditions	Coded Levels	Actual Levels	
Pressure (bar)	-1.00	250	
Passes	-1.00	1	
Concentration (%)	-1.00	30	
Response	Predicted Values	Experimental Values	Desirability
Particle size (nm)	403.45	**402.80**	1.00
Zeta potential (mV)	-15.59	**-12.40**	

$$\mathbf{Z=(Z_0-Z_c)/\Delta Z}$$

Where, Z and Z_0 indicate coded and actual levels of independent variables, respectively. ΔZ represents step change while Z_c indicated actual value at central point.

Desirability analysis (**Table 3.20**) validated the process, yielding a maximum desirability score of 1 at optimal conditions: 250 bar pressure, 1 pass, and 30% concentration. Predicted values for particle size and zeta potential were 403.45 nm and -15.59 mV, respectively, closely matching experimental results of 402.80 nm and -12.40 mV. Minimal deviations, supported by DLS data (**Fig. 3.19**), confirmed the accuracy of the predictions. These findings validate the reliability of the optimized parameters, demonstrating their suitability for further research and practical applications in nanocellulose production.

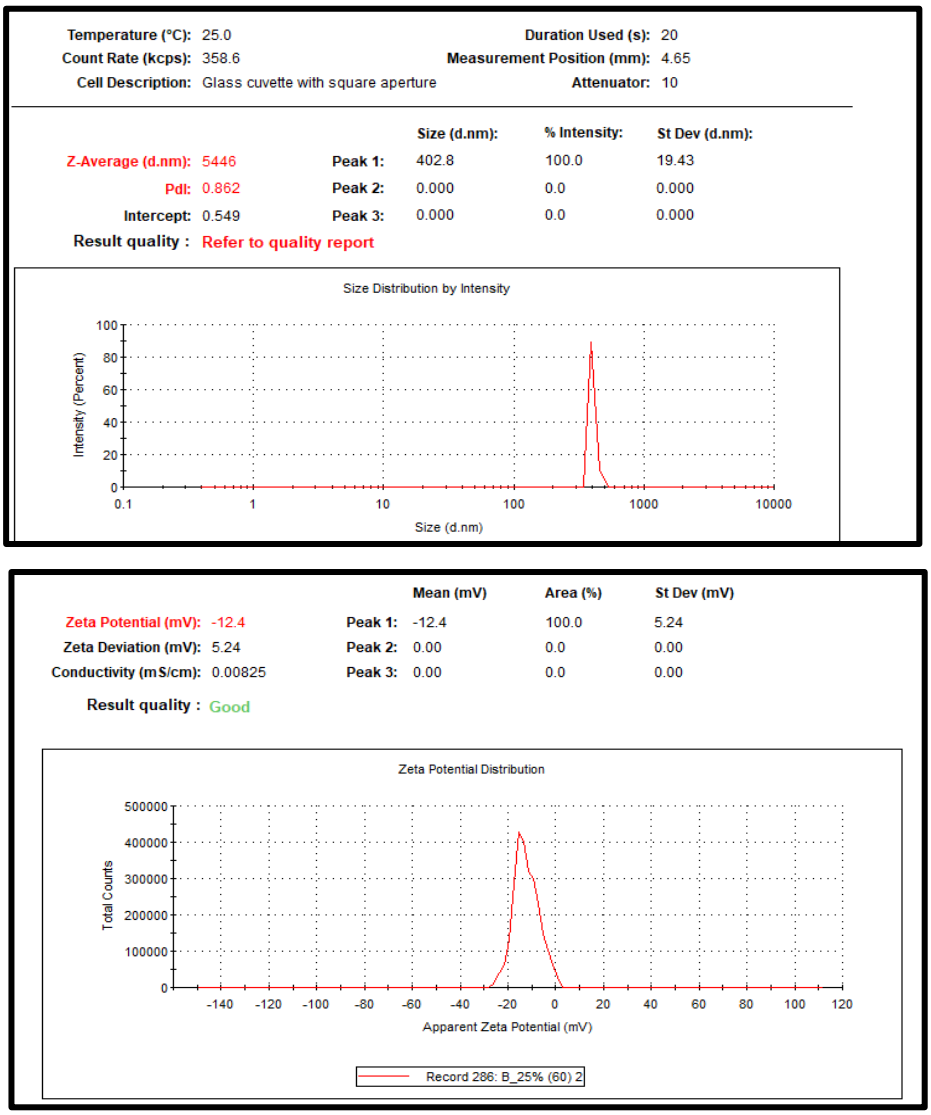

Fig. 3.19. Particle size and zeta potential of the nanocellulose obtained by high-pressure homogenization.

3.3.8. Characterisation of nanocellulose obtained from pineapple peel

3.3.8.1. Comparative analysis of the morphology of nanocellulose obtained by ultrasonication and high-pressure homogenisation

Fig. 3.20 provides a comprehensive analysis of nanocellulose derived from pineapple peel through various processing and characterization stages. **Fig. 3.20a** shows the dried cellulose sample as a lightweight pellet, demonstrating the effectiveness of tray drying in moisture removal, enhancing stability for storage and applications. In **Fig. 3.20b**, the nanocellulose suspension exhibits a translucent or milky appearance, characteristic of its nanoscale dimensions and high surface area. This uniform and stable dispersion confirms the successful isolation of nanocellulose through chemical and mechanical treatments, as well as the effective removal of non-cellulosic components and stabilization in the medium. **Fig. 3.20c** presents the SEM image of cellulose treated with ultrasonication. The image reveals morphological changes, such as ruptured surfaces and reduced fiber diameters, resulting from bleaching and acid hydrolysis. The long, narrow fibrils with uniform size reflect the successful conversion of cellulose into nanocellulose by removing non-cellulosic constituents. Conversely, **Fig. 3.20d** shows the SEM image of cellulose treated with high-pressure homogenization. This image depicts a rough, non-fibrillar surface without the organized, thread-like features observed in the ultrasonicated sample. This suggests that the homogenizer was less effective in breaking down the fibrillar structure. Based on these observations, ultrasonicated cellulose samples, which demonstrated superior morphological characteristics, were selected for further characterization.

(a) 

(b) 

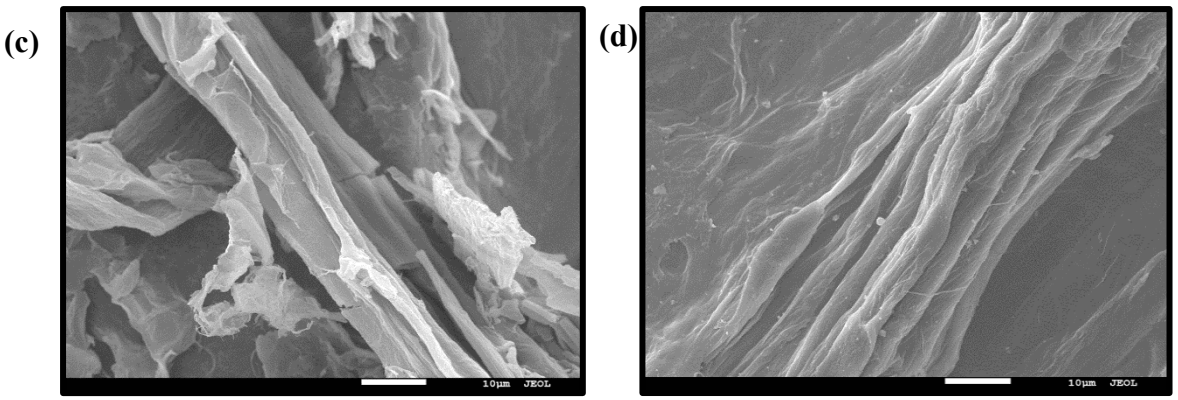

Fig. 3.20. (a) Images of cellulose, (b) nanocellulose obtained from pineapple peel, (c) SEM images of nanocellulose obtained from ultrasonication and (d) SEM images of nanocellulose obtained from high pressure homogenisation.

3.3.8.2. FTIR analysis of ultrasonicated samples

The chemical functionalities of raw pineapple peel powder, cellulose fibers, and nanocellulose (NC) were analysed using Fourier-transform infrared (FT-IR) spectroscopy, with the spectra presented in Fig. 3.21. The FT-IR analysis identified characteristic peaks corresponding to functional groups associated with lignocellulosic components, highlighting the chemical changes during the progressive treatment stages. The presence of hydroxyl groups is indicated by the broad peak at 3336 cm^{-1}, which is associated with the O-H stretching vibration. The C-H stretching vibration is responsible for the peak at 2894 cm^{-1}. These peaks are prominent across all samples, reflecting the cellulose backbone. A small peak at 1742 cm^{-1} was observed in the raw pineapple peel powder, associated with acetyl and uronic ester groups of hemicellulose, or the ester linkages of carboxylic acids (e.g., ferulic and p-coumaric acids) present in lignin and hemicellulose. This peak diminishes after chemical treatments, confirming the removal of lignin and hemicellulose. Additional tiny peaks at 1430, 1314, and 1256 cm^{-1} are associated with O-H deformation from phenolic groups, CH_2 rocking vibration at C6, and CH_2 scissoring motion in cellulose, respectively. Peaks related to cellulose-specific features appeared at 1205 cm^{-1} (C–O–C symmetric stretching), 1025 cm^{-1} (C–O–C pyranose ring stretching vibration), and 898 cm^{-1} (β-glycosidic linkages). The increased intensity and clarity of these peaks in NC demonstrate the effective removal of non-cellulosic components, such as hemicellulose and lignin, and confirm cellulose purification. These findings align with

reports by Camacho et al. (2017) and Anwar et al. (2021), underscoring the structural refinement achieved through chemical treatments.

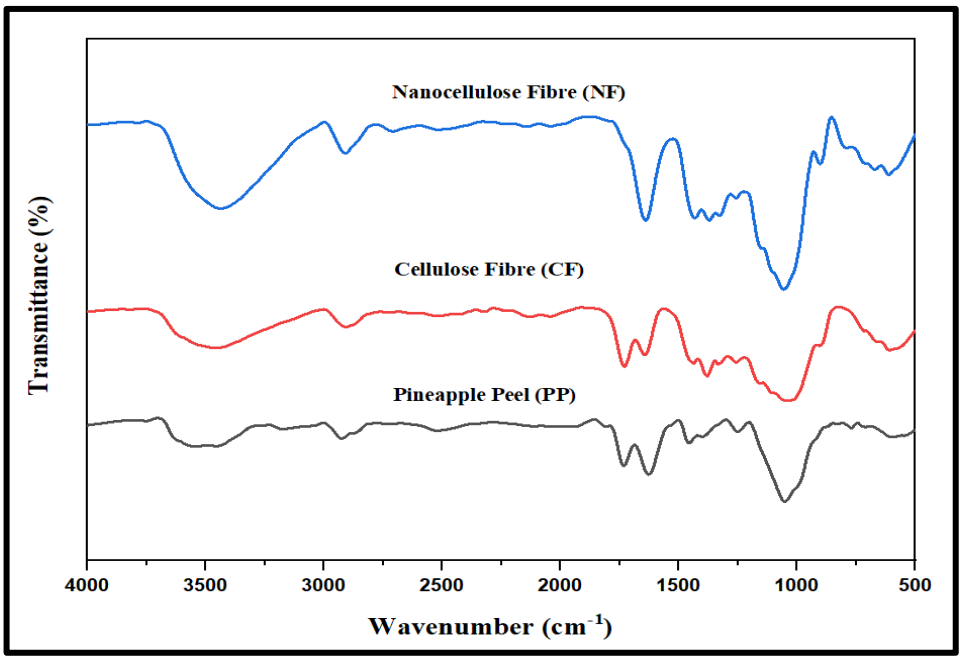

Fig. 3.21. FTIR spectra of powdered pineapple peel (PP), cellulose fibre (CF) and nanocellulose (NC).

3.3.8.3. Relative crystallinity of ultrasonicated samples

The X-ray diffraction (XRD) patterns of nanocellulose (NC) derived from pineapple peel at various treatment stages were analysed to study the effects of preparative conditions on crystallinity. The results, shown in **Fig. 3.22**, highlight the evolution of crystallinity from pineapple peel powder to cellulose fibers and finally to NC. The XRD patterns exhibited three prominent peaks at 2θ = 15°, 22°, and 34° in the final stage, corresponding to the crystalline structure of NC. Following bleaching and acid hydrolysis in stage 3, the peaks became more intense and narrower due to the effective removal of lignin, which contributed to enhanced crystallinity. A significant increase in the relative intensity of these peaks indicated a higher degree of crystallinity, consistent with typical nanocellulose properties, as supported by Dai et al. (2018) and Chen et al. (2021). The calculated relative crystallinity index for pineapple peel powder, cellulose fibers, and NC was 38%, 56.8%, and 61.3%, respectively. This increment resulted from the removal of lignin and the cleavage of cellulose molecular chains within the amorphous regions, exposing the crystalline domains. These findings confirm that chemical treatments improve the

structural order of NC, making it a promising material for applications requiring high crystallinity.

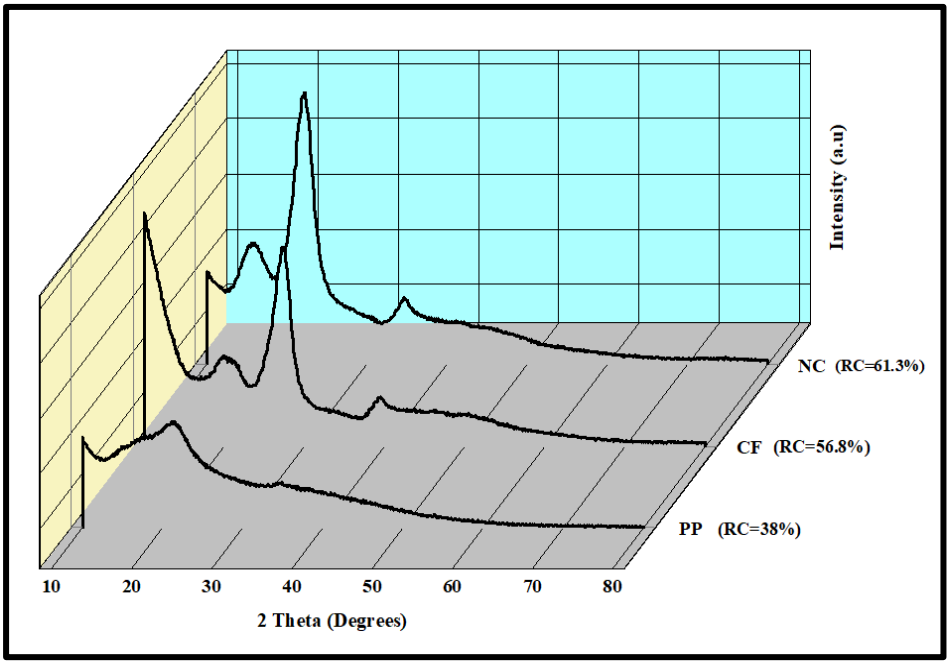

Fig. 3.22. X- ray diffraction of powdered pineapple peel (PP), cellulose fibre (CF) and nanocellulose (NC).

3.3.8.4. Thermogravimetric Analysis (TGA) and 1st order derivatives (DTG)

The thermal stability of the material was assessed by thermogravimetric analysis (TGA) for pineapple peel (PP), cellulose fibers (CF), and nanocellulose (NC) at different hydrolysis times. The TGA curves (**Fig. 3.23**) revealed an initial weight loss around 100 °C, attributed to water evaporation, represented by a slight negative slope at the beginning of the TG curve. The thermal stability of NC was generally higher than PP but showed a slight decrease in the initial decomposition temperature with varying hydrolysis times. This behaviour is linked to higher crystallinity and crystalline fraction, which improve thermal stability and increase degradation temperature (Camacho et al., 2017). PP exhibited lower thermal resistance compared to NC due to the insertion of sulfate groups during acid hydrolysis, which catalyse cellulose degradation. Additionally, the smaller particle size and higher surface area of PP contributed to its lower degradation temperature. In contrast, NC displayed higher thermal resistance due to increased crystallinity achieved through acid hydrolysis, as higher crystallinity correlates with enhanced thermal stability (Ouajai & Shanks, 2005). The major weight loss observed in NC was associated with the

degradation of cellulosic material, especially in the amorphous region. The addition of sulfate groups further reduced thermal stability in NC, as indicated by the steep slope of the TGA curve, reflecting its phase purity and quality (Mandal & Chakrabarty, 2011). These findings demonstrate that the chemical treatments effectively enhanced NC's crystalline structure, making it thermally more stable than untreated PP.

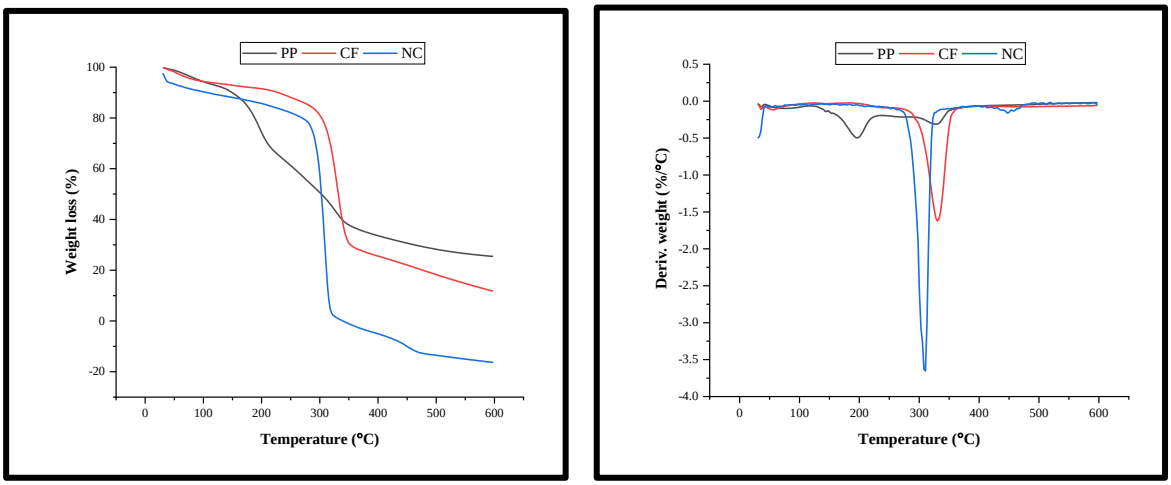

Fig. 3.23. Thermogravimetric analysis and 1ST derivatives (DTG) of pineapple peel (PP), cellulose fibre (CF) and nanocellulose (NC).

3.3.8.5. Differential scanning calorimetry (DSC) analysis of ultrasonicated samples

The heating DSC curves for pineapple peel powder, cellulose fiber, and nanocellulose, expressed in terms of heat flow, are shown in **Fig. 3.24a–c**, with the corresponding DSC analysis results summarized in **Table 3.21**. The initial endothermic peaks observed in the DSC curves are attributed to the evaporation of moisture or volatile components, a characteristic feature of materials containing bound water or solvents. Subsequent exothermic peaks represent thermal degradation or decomposition of organic components, providing insight into the thermal stability and breakdown behaviour of the materials at elevated temperatures (Shah et al., 2024). The thermal degradation properties of these materials were analysed in terms of onset temperatures, peak temperatures, and enthalpy of degradation (ΔH). Pineapple peel powder exhibited the lowest onset (40.0°C) and peak (55.3°C) temperatures, along with the minimal enthalpy of degradation (15.31 J/g), indicating its low thermal stability and weak structural integrity. In contrast, cellulose fiber demonstrated greater thermal stability, with two distinct peaks at 79.4°C and 335.3°C, and significantly higher enthalpy values (197.2 J/g and 32.28 J/g), reflecting improved

structural stability due to cellulose extraction. Nanocellulose, while showing a slightly lower onset temperature (35°C) and peak temperature (68.2°C) for the initial event compared to cellulose fiber, exhibited a markedly higher enthalpy for the second event (93.76 J/g). This highlights the enhanced crystallinity and thermal stability achieved through acid treatment. Overall, the results indicate that nanocellulose from pineapple peel possesses the highest thermal stability and structural resilience among the analysed materials, making it well-suited for applications requiring elevated temperature processing.

Table 3.21. Thermal parameters of raw and treated pineapple peel obtained from DSC analysis

Samples	Onset temperature (°C)	Peak temperature (°C)	Enthalpy of degradation (ΔH) (J/g)
Pineapple peel powder	40.0	55.3(endo)	15.31
Cellulose fibre	42.7	79.4 (endo)	197.2
	318.5	335.3 (endo)	32.28
Nanocellulose	35	68.2 (endo)	187.7
	307.7	327.4 (endo)	93.76

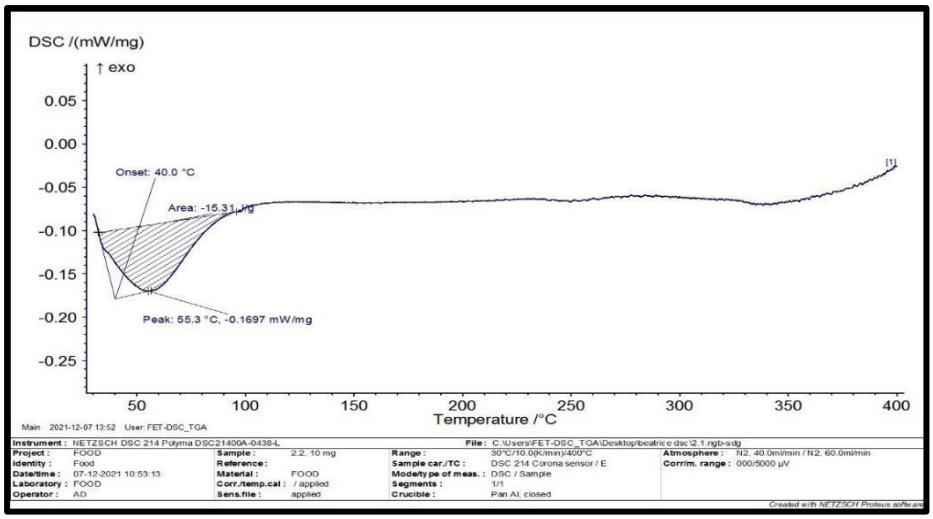

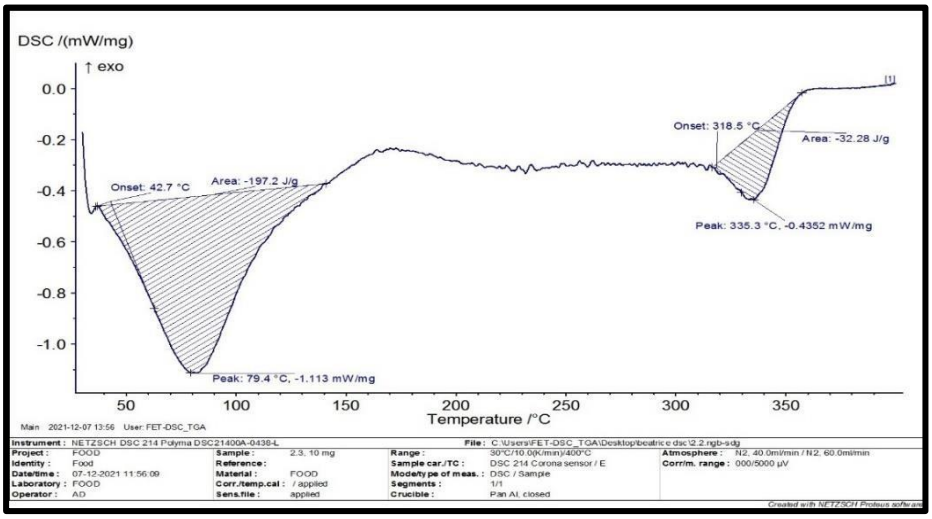

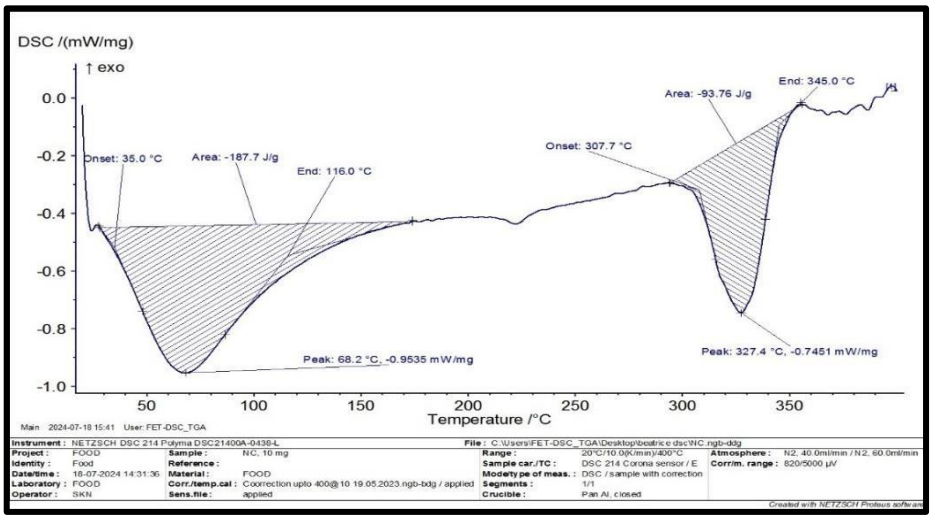

Fig. 3.24. DSC curve of raw (a) pineapple peel powder, (b) cellulose fibre and (c) nanocellulose.

3.3.8.6. TEM analysis of ultrasonicated nanocellulose

Transmission electron microscopy (TEM) images (**Fig. 3.25**) confirmed the successful isolation of nanocellulose (NC) following a series of chemical treatments applied to pineapple peel powder, including alkali treatment, bleaching, and acid hydrolysis. The alkali treatment effectively removed soluble components such as pectin, lignin, and hemicelluloses, while also purifying cellulose. Subsequent bleaching leached out phenolic compounds and residual lignin, and the final acid hydrolysis eliminated traces of minerals, residual carbohydrates, and amorphous cellulose, as reported by Sirohi et al. (2019). These treatments led to the formation of needle-like NC, evidenced by the TEM images, which also revealed a wire-like structure with partially individualized NC. This was attributed to the high specific surface area and strong hydrogen bonding between fibers. The TEM analysis further highlighted the presence of thin, round, tube-like nanostructures resembling nanotubes, which align with observations reported by Gopi et al. (2019). The nanocellulose exhibited nanoscale fibrils, a high aspect ratio (length-to-diameter ratio), and a few nanometers in length. The aspect ratio is a critical parameter for processing NC into composites with superior mechanical properties. Overall, the TEM results confirm the structural refinement and nanoscale morphology of NC obtained from pineapple peel, underscoring its potential for advanced material applications.

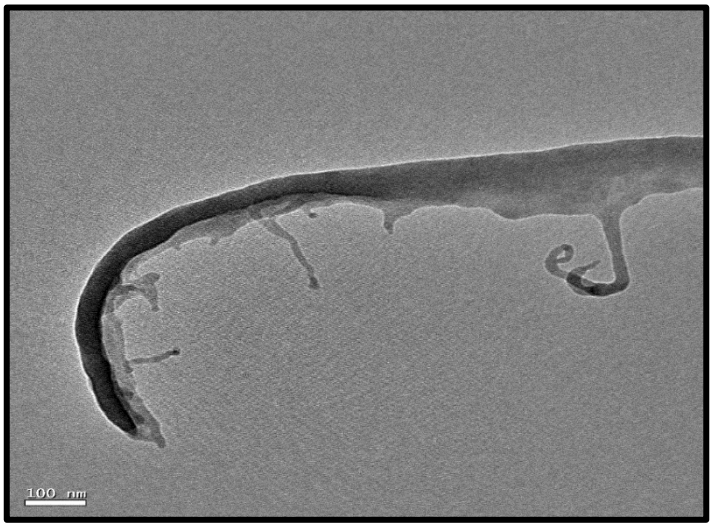

Fig. 3.25. TEM micrograph of the nanocellulose (NC).

3.3.8.7. AFM analysis of ultrasonicated nanocellulose

Accurate morphological examination of nanocellulose (NC) is essential, as its source and hydrolysis method significantly influence its dimensions and properties. Atomic force microscopy (AFM) analysis was performed to evaluate the morphology and size of NC extracted from pineapple peel powder, with topography images presented in **Fig. 3.26**. The AFM results confirm the successful production of needle-like NC with nanoscale fibrils, achieved through chemical treatments that effectively isolated NC from microsized fibers. Similar, observation was made in Dai et al. (2018). The rod-like, nanofibrillar network structure observed in the images highlights some degree of fibril aggregation and bundling due to hydrogen bonding and other intermolecular interactions. This aggregation poses challenges for precise size and aspect ratio measurements via AFM. Nevertheless, the analysis demonstrates the nanoscale dimensions of NC, indicating its potential utility in applications like composite materials and nanotechnology systems, where its unique structural and morphological properties can play a significant role.

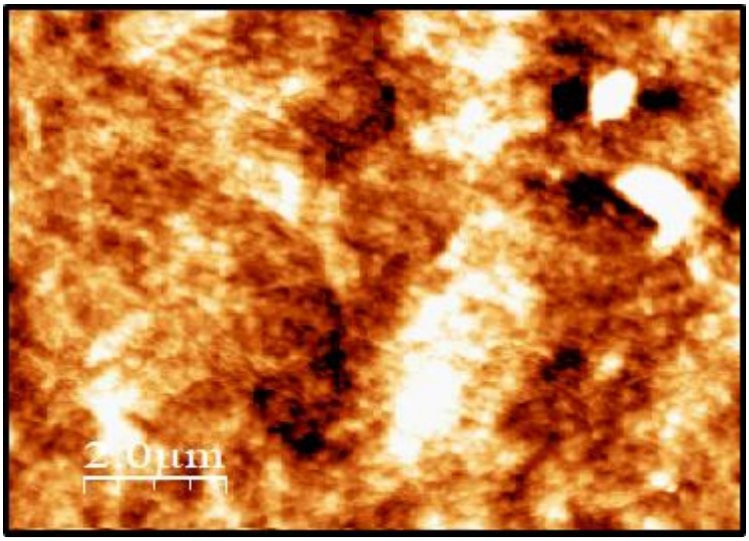

Fig. 3.26. AFM image of the nanocellulose (NC).

3.3.8.8. Component content comparison of banana rachis and pineapple peel

Table 3.22 highlights the composition of banana rachis and pineapple peel in terms of cellulose, hemicellulose, and lignin, which are critical in assessing their suitability for nanocellulose production and other applications. Banana rachis contains a significantly higher cellulose content (43.15%) compared to pineapple peel (21.81%), making it a superior raw material for cellulose-based products like nanocellulose, as cellulose is the

primary structural polymer that contributes to strength and crystallinity. The hemicellulose content is relatively comparable, with banana rachis at 33.42% and pineapple peel at 26.46%. Hemicellulose serves as a matrix material around cellulose fibers but contributes less to mechanical strength, necessitating its removal during purification processes. Additionally, banana rachis has a much higher lignin content (21.30%) compared to pineapple peel (6.50%). Lignin, a complex aromatic polymer, provides rigidity to plant cell walls but must be removed to isolate pure cellulose fibers. In summary, the higher cellulose and lignin content in banana rachis indicates greater potential as a raw material for cellulose extraction, although it requires more intensive delignification compared to pineapple peel.

Table 3.22. Component content of banana rachis and pineapple peel

Components	Banana rachis (%)	Pineapple peel (%)
Cellulose	43.15	21.81
Hemicellulose	33.42	26.46
Lignin	21.30	6.50

3.4. Conclusion

The optimization study reveals that nanocellulose isolated via ultrasonication yields superior results compared to high-pressure homogenization, particularly in terms of particle size and zeta potential. SEM imaging further supports these findings, showing that nanocellulose produced by ultrasonication exhibits a more fibrillar structure, whereas high-pressure homogenization results in a rough and irregular surface morphology. Additionally, the cellulose content in 100 g of banana rachis powder is significantly higher than in the same amount of pineapple peel powder. These observations highlight the effectiveness of ultrasonication for producing high-quality nanocellulose with desirable structural properties. Furthermore, banana rachis demonstrates greater potential as a source material for cellulose extraction due to its higher cellulose yield. This study underscores the importance of selecting appropriate processing methods and raw materials to optimize nanocellulose production, ensuring enhanced material properties for diverse applications in various food industries.